

# Isospin 0 and 2 two-pion scattering at physical pion mass using distillation with periodic boundary conditions in lattice QCD

M. Bruno

*Dipartimento di Fisica, Università di Milano-Bicocca, Piazza della Scienza 3, I-20126 Milano, Italy and INFN, Sezione di Milano-Bicocca, Piazza della Scienza 3, I-20126 Milano, Italy*

D. Hoying

*Albert Einstein Center, Institute for Theoretical Physics, University of Bern, Switzerland*

T. Izubuchi

*Physics Department, Brookhaven National Laboratory, Upton, NY 11973, USA and RIKEN-BNL Research Center, Brookhaven National Laboratory, Upton, NY 11973, USA*

C. Lehner

*Fakultät für Physik, Universität Regensburg, Universitätsstraße 31, 93040 Regensburg, Germany*

A. S. Meyer\*

*Physics Department, University of California, Berkeley, CA 94720, USA and Nuclear Science Division, Lawrence Berkeley National Laboratory, Berkeley, CA 94720, USA*

M. Tomii

*Physics Department, University of Connecticut, Storrs, CT 06269-3046, USA*  
(Dated: April 10, 2023)

The two pion channel in Lattice QCD has long been a primary testing ground for studying multiparticle scattering in finite volume QCD. With the development of sophisticated techniques such as distillation, it is possible to carefully study two-pion scattering in order to constrain associated low-energy constants. In this work, correlation functions with multiparticle interpolating operators are constructed to compute pion scattering phase shifts and scattering lengths in the isospin 0 and 2 channels with both sea and valence quarks at physical mass. Contamination from vacuum and thermal contributions are explicitly quantified with dedicated calculations and the results obtained after subtracting these nuisance terms are compared with the traditional correlator time series subtraction method. Two physical point ensembles with different lattice actions are used, and our finest ensemble gives results for scattering lengths and phase shifts consistent with phenomenology to within the reported statistical uncertainty.

## I. INTRODUCTION

With advances in computational techniques and increases in computing power have come ensembles with finer lattice spacings and physical pion masses. Paired with computational techniques such as distillation, Lattice QCD (LQCD) can now probe calculations of spectra and matrix elements involving multiparticle states. These advances are vital to obtain precise measurements of processes involving multiparticle scattering that are relevant for future and ongoing experiments, including predictions of CP violation in the kaon sector [1–5], exclusive channel studies for the reduction of statistical error in LQCD calculations of the hadronic vacuum polarization contribution to muon  $g - 2$  [6–9], and for isolating and removing excited state contamination in computations of nucleon form factors [10].

Scattering of pions is the primary testing ground for the LQCD multiparticle formalism. In LQCD, particle interactions in a finite volume prevent the separation of lattice states into their asymptotic free-particle states when the particles are separated by a large spatial distance. However, the power law corrections that are induced by the interactions between confined particles give access to the infinite volume scattering phase shift. The finite volume formalism of Lüscher [11–13] has been highly successful at describing two-particle states up to kinematic three- and four-particle thresholds, yielding predictions of the finite volume spectrum in good agreement with lattice results. Since its introduction in the seminal papers by Lüscher, the two-particle formalism has been expanded to include moving particles [14], unequal masses [15], coupled channels [16], nontrivial spin [17, 18], and even some three particle cases [19–21]. Additional work continues to improve the formalism with the goal of handling three-particle states in general and even a few calculations that have been completed using three-pion interpolating operators [22, 23]. Another method to compute the scattering phase shift using a

---

\* [asmeyer.physics@gmail.com](mailto:asmeyer.physics@gmail.com); Present address: Nuclear & Chemical Sciences Division, Lawrence Livermore National Laboratory, Livermore, CA 94550, USA

Bethe-Salpeter kernel also exists [24–26] and has been used to compute  $\pi\pi$  scattering phase shifts [27], but this method will not be explored in this analysis.

Studying pion scattering with distillation [28] has the additional advantage of allowing simple computations of pion transition matrix elements without the need for additional propagator solves. These improvements allow for the explicit subtraction of nuisance terms associated with propagating single-pion states that contribute to thermal corrections to the two-pion correlation functions. Thermal terms are often treated as negligible due to an exponential suppression in the temporal extent, an assumption that is testable with the distillation framework. Distillation is also used to access the vacuum contributions to the correlation functions, which manifest as a large constant term in the correlation function.

This document is organized as follows. In Sec. II, we discuss the methods used in this analysis. This includes a brief discussion of distillation and its implementation in this project. In addition, we discuss our method for dealing with vacuum contributions to the isospin 0 channel and states that appear from the finite temporal boundary condition effects as well as a technique to improve the statistical uncertainty on our correlation functions. Section III discusses the lattice setup, including the ensembles used and some of the computational details. In Sec. IV, we apply the techniques outlined in Sec. II to extract the spectrum of states from our data. The observed spectra are used in Sec. V with the Lüscher formalism to compute and fit the lowest partial wave scattering phase shifts and scattering lengths for the isospin 0 and isospin 2 channels. In Sec. VI, we give results from fitting the phase shift curves and conclude. In Appx. A, we go through the details of the Lüscher formalism and the relation between the spectrum and scattering phase shift. In particular, we write this relation in a basis-independent scheme to make the remnant rotational symmetry of the formalism manifest.

## II. METHODS

The numerical techniques in this study seek to construct a Hermitian matrix correlator with propagating two-pion states. A two-point function matrix correlator will have a general parametric form

$$\begin{aligned} C_{AB}(t) &= \langle \mathcal{O}_A(t) \mathcal{O}_B^\dagger(0) \rangle \\ &= \sum_{mn} \langle m | \mathcal{O}_A | n \rangle \langle n | \mathcal{O}_B^\dagger | m \rangle e^{-E_n t} e^{-E_m(T-t)}, \end{aligned} \quad (1)$$

which contains the desired two-pion states as well as other unwanted contributions from the vacuum, one-pion states, or other higher excitations. The large basis of operators used for the indices  $A$  and  $B$  is obtained from quark propagators obtained using the distillation methodology, which is outlined in Sec. II A. The construction of correlation functions from distillation propagators

and the projection of the interpolating operators to definite isospin quantum numbers is detailed in Sec. II B.

The spectrum of states in the matrix correlator will be obtained by solving the Generalized EigenValue Problem (GEVP), which is outlined in Sec. II C. The GEVP assumes a generic form

$$C_{AB}(t) = \sum_{n>0} \langle 0 | \mathcal{O}_A | n \rangle \langle n | \mathcal{O}_B^\dagger | 0 \rangle e^{-E_n t}, \quad (2)$$

which does not contain any terms with states propagating through the periodic temporal boundary condition. These unwanted “thermal” states are removed by performing a supplemental calculation of three-point correlation functions to obtain matrix elements of the form  $\langle m | \mathcal{O}_A | n \rangle$  and then subtracting the corresponding thermal contribution in the two-point function. This procedure is described in Sec. II D. Additional contributions to Eq. (2) from purely vacuum terms in the isospin 0 channel can also be subtracted by using vacuum matrix elements  $\langle 0 | \mathcal{O}_A | 0 \rangle$  from one-point correlation function data, described in Sec. II E. With both of these additional matrix elements computed, Eq. (2) may be obtained from Eq. (1) with the subtractions

$$\begin{aligned} C_{AB}(t) &= \mathcal{C}_{AB}(t) - \langle 0 | \mathcal{O}_A | 0 \rangle \langle 0 | \mathcal{O}_B^\dagger | 0 \rangle \\ &\quad - \sum_{m>0, n>0} \langle m | \mathcal{O}_A | n \rangle \langle n | \mathcal{O}_B^\dagger | m \rangle e^{-E_n t} e^{-E_m(T-t)}, \end{aligned} \quad (3)$$

where  $m > 0$  in the sum denotes all states except for the vacuum state.

After the spectrum of states is obtained through application of the GEVP, the scattering phase shifts and scattering lengths are computed by applying the Lüscher quantization condition. This procedure is outlined in Sec. II F, with more detail given in Appendix A. An improvement to the momentum inputs to the Lüscher quantization, which uses linear combinations of single-pion correlation functions to obtain the interacting-minus-noninteracting difference of energies in the two-pion system, is explained in Sec. II G. The scattering lengths and phase shifts obtained from the interacting-noninteracting energy differences are used to produce the results in Sec. V.

The states in this manuscript are schematically labeled as one-pion ( $|\pi\rangle$ ), two-pion ( $|\pi\pi\rangle$ ), or vacuum ( $|0\rangle$ ) based on the tower of states that is expected. Though this nomenclature is suggestive of the spectrum of states that should be expected in each channel, the restriction to finite volume complicates this picture. The reader should use caution when identifying the discrete finite volume states with the corresponding asymptotic states in infinite volume. Instead of being an exact identification of the asymptotic states, these labels are instead meant to represent states that transform under distinct representations of the symmetries of the system restricted to finite volume.

### A. Distillation

Generation of the many  $\pi\pi$  correlation functions used in this project is made simpler using the common technique in LQCD known as distillation [28]. Distillation makes use of the eigenvectors of some operator, typically chosen to have strong overlap with the lowest-energy states in the spectrum. The eigenvectors are constructed to satisfy the eigenvalue equation

$$\sum_{\mathbf{y}} \Delta(\mathbf{x}, \mathbf{y}) V^n(\mathbf{y}) = V^n(\mathbf{x}) \lambda^n, \quad (4)$$

where the eigenvalues are ordered such that  $\lambda^m \geq \lambda^n$  for  $m > n$ .

The most commonly used operator is the discrete spatial Laplace operator, which in a three-dimensional spatial volume is given by

$$\Delta_{\mathbf{x}, \mathbf{y}} = -\delta_{\mathbf{x}, \mathbf{y}} + \frac{1}{6a^2} \sum_i (U_i(\mathbf{x}) \delta_{\mathbf{x}, \mathbf{y} - a\hat{i}} + U_i^\dagger(\mathbf{x} - a\hat{i}) \delta_{\mathbf{x}, \mathbf{y} + a\hat{i}}) \quad (5)$$

for discrete spacetime, where color indices and time-slices have been suppressed. The Laplacian is intuitively a good choice because the free-field eigenmodes of the Laplacian are plane waves, with the lowest state corresponding to a particle at rest, and higher eigenmodes to particles with more momentum.

The eigenvectors of the distillation operator are provided as sources for solving the Dirac equation for Green's function  $G$ ,

$$\sum_{y_4, \mathbf{y}} \mathcal{D}(x_4, \mathbf{x}, y_4, \mathbf{y}) G^n(y_4, x_4, \mathbf{y}) = V^n(x_4, \mathbf{x}) \quad (6)$$

with both spinor and color indices suppressed. Here, the distillation eigenvectors  $V$  are now given an explicit Euclidean time index  $x_4$ . The eigenvectors  $V$  are assumed to be diagonal in the spinor indices so that spin representations are not mixed up by the application of eigenvectors. After solving, the Green's function is contracted with a conjugate eigenvector to create a ‘‘perambulator’’,

$$\mathcal{G}^{mn}(y_4, x_4) = \sum_{\mathbf{y}} [V^m(y_4, \mathbf{y})]^\dagger G^n(y_4, x_4, \mathbf{y}), \quad (7)$$

where now all dependence on spatial positions has been subsumed by the eigenvector indices. The perambulators still satisfy many of the same symmetry transformations as propagators, most importantly  $\gamma_5$  hermiticity:

$$\gamma_5 [\mathcal{G}^{mn}(x_4, y_4)]^\dagger \gamma_5 = \mathcal{G}^{nm}(y_4, x_4). \quad (8)$$

This property will be especially important for assessing how bias corrections may be performed in Sec. III C.

Eq. (7) has the advantage over traditional methods of sequential inversions in that any dependence on the spatial position is encoded in the eigenvector number. This

means the perambulator objects are smaller than traditional propagators and the perambulators can be contracted without the need for large amounts of computational resources. Additionally, the contractions of more quark lines amount to additional matrix multiplications, meaning that the same set of perambulators may be used to construct arbitrary  $N$ -point correlation functions without the need for additional solutions to the Dirac matrix. This advantage has been vital for constructing the two-pion correlation functions in this analysis.

### B. Interpolating Operator Construction

If the eigenspectrum of the distillation operator is truncated at some finite number of eigenvectors  $N$ , the subset of eigenvectors form a projection matrix,

$$\sum_n^N V^n(\mathbf{x}) [V^n(\mathbf{y})]^\dagger = \mathcal{P}(\mathbf{x}, \mathbf{y}). \quad (9)$$

This projection matrix acts by smearing out the field on a lattice timeslice. Then interpolating operators may be constructed by applying the projections to the quarks and Fourier phase,

$$\mathcal{O}_{i,j,\Gamma,\mathbf{P}} = \sum_{\mathbf{x}, \mathbf{y}, \mathbf{z} \in L^3} \bar{\psi}_i(\mathbf{x}) \mathcal{P}(\mathbf{x}, \mathbf{y}) \Gamma e^{-i\mathbf{P} \cdot \mathbf{y}} \mathcal{P}(\mathbf{y}, \mathbf{z}) \psi_j(\mathbf{z}), \quad (10)$$

where  $i$  and  $j$  are flavor indices,  $\Gamma$  is a gamma spin matrix, and  $\mathbf{P}$  is the momentum of the bilinear. If the eigenvectors are contracted over their spacetime indices, elements may be constructed of the form

$$\tilde{\mathcal{P}}^{mn}(x_4, \mathbf{p}) \equiv \sum_x [V^m(x_4, \mathbf{x})]^\dagger e^{-i\mathbf{p} \cdot \mathbf{x}} V^n(x_4, \mathbf{x}), \quad (11)$$

which may be used to construct, for example, the pion two-point function,

$$\begin{aligned} \langle \mathcal{O}_{\pi, \mathbf{p}}(t) \mathcal{O}_{\pi, \mathbf{p}}(0) \rangle = & \sum_{m, m', n, n'} \left\langle \text{Tr} \left[ \mathcal{G}^{mn}(t, 0) \gamma_5 \tilde{\mathcal{P}}^{nn'}(t, \mathbf{p}) \right. \right. \\ & \left. \left. \times \mathcal{G}^{n'm'}(0, t) \gamma_5 \tilde{\mathcal{P}}^{m'm}(0, \mathbf{p}) \right] \right\rangle. \end{aligned} \quad (12)$$

The quark spinors  $\psi$  in Eq. (10) are assumed to be a 2-vector with isospin-symmetric up and down flavors,

$$\psi = \begin{pmatrix} u \\ d \end{pmatrix}, \quad \bar{\psi}^T = \begin{pmatrix} \bar{d} \\ -\bar{u} \end{pmatrix}. \quad (13)$$

Isospin 0 and isospin 1 bilinears for the interpolating operators are constructed by contracting with Clebsch-

Gordan coefficients to pull out the  $I_z = 0$  component,

$$\begin{aligned} \mathcal{I}_{i,j}^{(0,0)} &= \frac{1}{\sqrt{2}} \begin{pmatrix} 0 & -1 \\ 1 & 0 \end{pmatrix} \\ \implies \sum_{i,j} \mathcal{I}_{i,j}^{(0,0)} \mathcal{O}_{i,j} &\sim \frac{1}{\sqrt{2}} (\bar{d}d + \bar{u}u), \end{aligned} \quad (14)$$

and

$$\begin{aligned} \mathcal{I}_{i,j}^{(1,0)} &= \frac{1}{\sqrt{2}} \begin{pmatrix} 0 & 1 \\ 1 & 0 \end{pmatrix} \\ \implies \sum_{i,j} \mathcal{I}_{i,j}^{(1,0)} \mathcal{O}_{i,j} &\sim \frac{1}{\sqrt{2}} (\bar{d}d - \bar{u}u). \end{aligned} \quad (15)$$

The  $\pm 1$  components of the isospin 1 representation are obtained from

$$\mathcal{I}_{i,j}^{(1,\pm 1)} = \frac{1}{2} (\delta_{i,j} \pm \sigma_{i,j}^3), \quad (16)$$

with the Pauli spin matrix  $\sigma^3$ . This analysis makes use of both the scalar isospin 0 bilinear with zero center of mass momentum,

$$\mathcal{O}_1 = \sum_{i,j} \mathcal{I}_{i,j}^{(0,0)} \mathcal{O}_{i,j,1,0}, \quad (17)$$

and the moving  $1\pi$  operator,

$$\mathcal{O}_{\pi, \mathbf{p}\pi}^{(1,k)} = \sum_{i,j} \mathcal{I}_{i,j}^{(1,k)} \mathcal{O}_{i,j,\gamma_5, \mathbf{p}\pi}. \quad (18)$$

The  $\pi\pi$  interpolating operators are then composite operators built from the  $1\pi$  bilinears with equal and opposite relative momentum  $\mathbf{p}_{\text{rel}}$  and isospin component  $I_z = 0$ ,

$$\begin{aligned} \mathcal{O}_{\pi\pi}^{(I,0)} &\left( \left| \frac{\mathbf{p}_{\text{rel}} L}{2\pi} \right|^2 \right) \\ &= \frac{1}{\sqrt{N_{\{\mathbf{p}_{\text{rel}}\}}}} \sum_{i,j} \sum_{\mathbf{p} \in \{\mathbf{p}_{\text{rel}}\}} \mathcal{I}_{i,j}^{(\pi\pi, I, 0)} \mathcal{O}_{\pi, \mathbf{p}}^{(1,i)} \mathcal{O}_{\pi, -\mathbf{p}}^{(1,j)}, \end{aligned} \quad (19)$$

where  $\{\mathbf{p}_{\text{rel}}\}$  is the set of momenta that can be obtained by applying cubic group rotations to  $\mathbf{p}_{\text{rel}}$  and  $N_{\{\mathbf{p}_{\text{rel}}\}}$  is the total number of momenta in  $\{\mathbf{p}_{\text{rel}}\}$ ,

$$N_{\{\mathbf{p}_{\text{rel}}\}} = \sum_{\mathbf{p} \in \{\mathbf{p}_{\text{rel}}\}} 1. \quad (20)$$

The  $\pi\pi$  interpolating operators in Eq. (19) are implicitly constructed to transform under the trivial representation of the cubic rotation group, so will couple primarily to  $\ell = 0$  states. Working in a basis where the first, second, and third rows correspond to the  $\pi^+$ ,  $\pi^0$ , and  $\pi^-$ , respectively, the  $\pi\pi$  isospin factors are

$$\begin{aligned} \mathcal{I}^{(\pi\pi, 0, 0)} &= \frac{1}{\sqrt{3}} \begin{pmatrix} 0 & 0 & 1 \\ 0 & -1 & 0 \\ 1 & 0 & 0 \end{pmatrix}, \\ \mathcal{I}^{(\pi\pi, 2, 0)} &= \frac{1}{\sqrt{6}} \begin{pmatrix} 0 & 0 & 1 \\ 0 & 2 & 0 \\ 1 & 0 & 0 \end{pmatrix} \end{aligned} \quad (21)$$

for the isospin 0 and isospin 2 representations, respectively.

### C. Generalized Eigenvalue Problem

The Generalized EigenValue Problem (GEVP) [29, 30] is a technique for computing the spectrum of states from a matrix of correlation functions without the need to fit. A diagonal eigenvalue matrix  $\Lambda$  is obtained from solving the GEVP equation,

$$C(t)V = C(t_0)V\Lambda. \quad (22)$$

The matrix  $C_{AB}(t)$  is a square, symmetric matrix of correlation functions, with source and sink operators indexed by  $A$  and  $B$ , respectively, which run from 0 to  $N-1$  for  $N$  operators. The GEVP makes the assumption that the correlation functions are a sum of exponentials,

$$C_{AB}(t) = \sum_n \langle 0 | \mathcal{O}_A | n \rangle \langle n | \mathcal{O}_B^\dagger | 0 \rangle e^{-E_n t}. \quad (23)$$

If the sum is truncated at finite  $N$ , where  $N$  matches the rank of the matrix  $C(t)$ , then the eigenvalue matrix obtained from solving the GEVP is exactly

$$\Lambda_{mn}(t_0, t) = \delta_{mn} e^{-E_n(t-t_0)}. \quad (24)$$

If the number of states is  $M > N$ , then the eigenvalues receive exponential corrections from the higher states in the spectrum. The form of Eq. (24) is recovered in the asymptotic limit of  $t_0, t \rightarrow \infty$ .

The usual strategy for computing the GEVP is to fix  $t_0$  and compute the eigenvalues by varying  $t$  for  $t > t_0$ . However, the excited state contamination is primarily driven by the smaller of the two timeslices, or  $t_0$  for this choice of ordering. Fixing  $t_0$  hides the excited state contamination, making for plots that are deceptively flat for increasing  $t$  and small  $t_0$  despite a nonnegligible contamination. For this reason, we choose to instead fix  $\delta t = t - t_0$  and vary  $t_0$ . It should be understood that this is simply a change of parameters in the context of the GEVP and any arguments about excited state contamination and asymptotic convergence of the GEVP in Ref. [29] will still hold. Keeping  $t_0 \geq \delta t$  ensures that the condition  $t_0 \geq t/2$  is satisfied.

One difficulty with the GEVP is the issue of eigenvalue sorting. Nearby states with overlapping uncertainties and statistical fluctuations in data can make sorting of states according to their eigenvalues ambiguous. To deal with this, the eigenvector sorting algorithm of Ref. [31] is employed, which assigns a score to every permutation of eigenvectors  $\epsilon$  according to the metric

$$c_\epsilon(t, t') = \prod_k \left| \det [V_0(t'), \dots, V_{k-1}(t'), V_k(t), V_{k+1}(t'), \dots, V_{N-1}(t')] \right| \quad (25)$$

for sorting of eigenvectors on timeslice  $t$  according to the reference vectors on timeslice  $t'$ . The permutation  $\epsilon$  that maximizes the score  $c_\epsilon(t, t')$  is taken as the optimal choice. This metric favors orderings where eigenvector  $V_k(t)$  on the target timeslice is maximally orthogonal to the eigenvectors  $V_{k' \neq k}(t')$  on the reference timeslice.

#### D. Thermal Contributions to Two-Pion Correlators

Correlation functions for the typical two-point  $\pi\pi$  operators in general will contain not only the contributions from the propagating two-pion states, but also an unwanted contribution from a single pion that propagates through the temporal periodic boundary condition. The two-point correlation function can be written as

$$\begin{aligned} \mathcal{C}_{AB}(t) &= \sum_n \langle 0 | \mathcal{O}_A | n \rangle \langle n | \mathcal{O}_B^\dagger | 0 \rangle e^{-E_n t} \\ &+ \sum_{m' > 0, m} \langle m' | \mathcal{O}_A | m \rangle \langle m | \mathcal{O}_B^\dagger | m' \rangle e^{-E_m t} e^{-E_{m'}(T-t)}, \end{aligned} \quad (26)$$

where the sums are taken over various choices of discrete lattice momenta. The first term of the right-hand side is the desired correlation function, and the second term is a nuisance term involving  $1\pi$  transition matrix elements that must be estimated and subtracted away.

The expected number of state energies below some energy cutoff for the two-pion correlation functions can be estimated by counting distinct combinations of momenta. Momenta that are related by discrete lattice rotations give degenerate spectra and therefore count toward a single state energy. In the center-of-mass frame, at least one state contributes for each choice of magnitude for the back-to-back relative pion momenta and are schematically represented as

$$|n\rangle \sim \sum_{\mathbf{p}_{\text{rel}}} |\pi(\mathbf{p}_{\text{rel}})\pi(-\mathbf{p}_{\text{rel}})\rangle. \quad (27)$$

In this schematic notation, the sum runs over momenta related by rotations. This counting neglects states that may appear with additional particles or different particle content, and additional states may also appear when the interaction channel exhibits a resonance. Higher-energy terms in the two-pion correlation functions that might result from excited states with other particle contents are treated as negligible due to their exponential mass suppression and no speculation is made about their content.

In the center of mass frame, the one-pion thermal terms can include any discrete momentum state

$$|m\rangle, |m'\rangle \sim |\pi(\mathbf{p}_\pi)\rangle \quad (28)$$

with  $|\mathbf{p}_\pi L/2\pi|^2 \in \mathbb{Z}$ , so long as  $m = m'$  to conserve momentum. Higher terms again might be present and are neglected. The states  $m$  and  $m'$  in these thermal terms also sum over pions in an isospin triplet. In general, matrix elements involving  $\pi^\pm$  states do not contribute the same as  $\pi^0$  states. For the isospin-2 channel in particular, using isospin  $z$ -component equal 0 operators,

$$\langle \pi^\pm | \mathcal{O}_{2,0} | \pi^\pm \rangle = -\frac{1}{2} \langle \pi^0 | \mathcal{O}_{2,0} | \pi^0 \rangle. \quad (29)$$

For the isospin-0 channel, the prefactor is trivial,

$$\langle \pi^\pm | \mathcal{O}_{0,0} | \pi^\pm \rangle = \langle \pi^0 | \mathcal{O}_{0,0} | \pi^0 \rangle. \quad (30)$$

For consistency, the  $\pi^\pm$  contributions are converted to the  $\pi^0$  contribution by applying Wigner-Eckart theorem. The corresponding isospin prefactors on the thermal contributions are then 3 and  $\frac{3}{2}$  for the isospin 0 and 2 channels, respectively. An additional prefactor counting the number of momenta,  $N_{\{\mathbf{p}_{\text{rel}}\}}$  from Eq. (20), is also included to account for all possible momenta.

Although the thermal contributions can be sizeable for the spin-singlet representation at zero center-of-mass momentum, the thermal contributions may be removed by subtracting timeslices of the matrix correlation function, such as

$$C'(t; dt) = C(t - dt) - C(t), \quad (31)$$

with fixed  $dt$ . While this subtraction does remove the offending thermal contributions, it also increases the statistical noise of the desired  $\pi\pi$  contribution at timeslice  $t$  and enhances the effects of excited states relative to the ground state. This subtraction is also only exact for the  $\pi\pi$  operators with zero total center-of-mass momentum, i.e. the rest frame. For the moving frames, alternate subtraction schemes must be employed to account for the unequal masses of the two one-pion states and these subtraction schemes will not exactly cancel all of the thermal terms.

A unique feature of the distillation setup is the ability to easily compute the contributions from thermal terms. These terms are particularly problematic in the S-wave representation of the isospin 0 and isospin 2 channels, where it is possible to resolve the  $1\pi$  contribution that propagates through the temporal extent of the lattice. The transition matrix elements relating the  $\pi\pi$  operators to the  $1\pi$  states,  $\langle \pi | \mathcal{O}_{\pi\pi} | \pi \rangle$ , can be obtained from a three-point function constructed with one-pion operators at the source and sink,

$$\begin{aligned} \mathcal{C}_{3,A,\mathbf{p}_\pi}(t, \tau) &= \langle \mathcal{O}_{\pi,\mathbf{p}_\pi}(t) \mathcal{O}_A(\tau) \mathcal{O}_{\pi,\mathbf{p}_\pi}^\dagger(0) \rangle \\ &= \sum_{mm'} \langle 0 | \mathcal{O}_{\pi,\mathbf{p}_\pi} | m \rangle \langle m | \mathcal{O}_A | m' \rangle \langle m' | \mathcal{O}_{\pi,\mathbf{p}_\pi}^\dagger | 0 \rangle \\ &\quad \times e^{-E_m(t-\tau)} e^{-E_{m'}\tau} + O(e^{-M_\pi(T-t)}), \end{aligned} \quad (32)$$

where the  $1\pi$  spectrum and matrix elements can be easily obtained from a one-pion two-point function. The  $1\pi$  operators are given in Eq. (18). An explicit computation of these transition matrix elements can give insight about the size of the thermal contributions compared to the contributions from the desired  $\pi\pi$  state propagation.

After obtaining the transition matrix elements from a dedicated study, the thermal terms can be effectively removed from the  $\pi\pi$  correlation functions. Assuming no

vacuum contribution, the subtraction is defined by

$$\begin{aligned}
C_{AB}(t) &= \langle \mathcal{O}_A(t) \mathcal{O}_B^\dagger(0) \rangle \\
&- \sum_{m>0, n>0} \langle n | \mathcal{O}_A | m \rangle \langle m | \mathcal{O}_B^\dagger | n \rangle e^{-E_m t} e^{-E_n(T-t)}.
\end{aligned} \tag{33}$$

Subtraction of thermal contributions gives better statistical precision than time series subtraction schemes without introducing large systematic corrections. In calculations with moving frame data, explicit calculation of the transition matrix elements can give a more rigorous approach to removing thermal effects than an approximate subtraction scheme [32]. To distinguish between these two schemes of removing contamination from vacuum and thermal contributions, we adopt the following nomenclature:

**“Time series subtraction”:** Application of Eq. (31) to generally subtract contamination, and

**“Matrix element subtraction”:** Application of some combination of Eqs. (33) and (36)–(38) to subtract away specific contamination that is expected in the correlation functions.

### E. Vacuum Contributions to Two-Pion Correlators

In addition to the thermal corrections of the previous subsection, the isospin 0 channel in the center of mass frame also contains contributions from vacuum matrix elements,

$$\begin{aligned}
\mathcal{C}_{AB}(t) &= \sum_{n>0} \langle 0 | \mathcal{O}_A | n \rangle \langle n | \mathcal{O}_B^\dagger | 0 \rangle e^{-E_n t} \\
&+ \sum_{m'>0, m} \langle m' | \mathcal{O}_A | m \rangle \langle m | \mathcal{O}_B^\dagger | m' \rangle e^{-E_m t} e^{-E_{m'}(T-t)} \\
&+ \langle 0 | \mathcal{O}_A | 0 \rangle \langle 0 | \mathcal{O}_B^\dagger | 0 \rangle.
\end{aligned} \tag{34}$$

The vacuum matrix element can be obtained from a one-point correlation function,

$$\mathcal{C}_{1,A} \equiv \langle \mathcal{O}_A \rangle = \langle 0 | \mathcal{O}_A | 0 \rangle + \sum_{m>0} \langle m | \mathcal{O}_A | m \rangle e^{-E_m T}, \tag{35}$$

where the second term on the right hand side is a thermal contribution to the one-point function from thermal states propagating through the periodic boundary conditions.

Though in principle any momentum can appear for a  $1\pi$  state thermal term, in practice the exponential suppression is sufficient to remove all but the 0-momentum contribution. Like the thermal terms, summing over  $m$  also produces an isospin factor to account for a triplet

of pions propagating through the periodic boundary condition. From Eq. (30), this scales the transition matrix element for  $\pi^0$  by 3.

The vacuum matrix element contributions tend to be statistically noisy, so it is beneficial to take advantage of statistical cancellation by correlating the vacuum contributions with the  $\pi\pi$  two-point functions timeslice-by-timeslice. The vacuum matrix element first has the thermal term removed (retaining the  $t$ -dependence of the vacuum term but taking the time-averaged thermal contribution),

$$C_{1,A}(t) \equiv \mathcal{C}_{1,A}(t) - \sum_{m>0} \langle m | \mathcal{O}_A | m \rangle e^{-E_m T}. \tag{36}$$

A subtracted two-point correlation function can be formed to remove the vacuum matrix element, correlating the times of the two-point functions with those of the one-point function,

$$\begin{aligned}
C_{AB}(t, t_0) &\equiv \\
&\langle \mathcal{O}_A(t+t_0) \mathcal{O}_B^\dagger(t_0) \rangle - C_{1,A}(t+t_0) C_{1,B}(t_0).
\end{aligned} \tag{37}$$

After this correction, Eq. (37) is averaged over  $t_0$  and the remaining thermal term for the two-point function is subtracted away,

$$\begin{aligned}
C_{AB}(t) &\equiv \frac{1}{T} \sum_{t_0} C_{AB}(t, t_0) \\
&- \sum_{m>0, n>0} \langle n | \mathcal{O}_A | m \rangle \langle m | \mathcal{O}_B^\dagger | n \rangle e^{-E_m t} e^{-E_n(T-t)}.
\end{aligned} \tag{38}$$

Combining all of these steps yields a correlation function that contains only the two-pion contributions of interest.

### F. Scattering Phase Shift Formalism

The  $\pi\pi$  scattering phase shift is computed from the energy spectrum in the finite, periodic volume assuming the center-of-mass energy is small enough that the pions elastically scatter with each other. Large shifts in energy are possible due to finite periodic volume that the pions are confined to. These energy shifts are the result of pions being unable to exist in wavefunctions that are asymptotically separated from each other, resulting in reinteractions as the particles traverse the periodic boundary conditions. This energy shift can be expressed as a power-law correction to the two-particle spectrum states, unlike the usual exponential corrections that are seen for one-particle states. In this section, only the most important formulae for computing the scattering phase shifts will be given. A more detailed derivation has been performed in Appendix A.

The derivation of the scattering phase shift relation comes from solving the determinant equation

$$\det \left[ e^{2i\delta(q)} - U(q) \right] = 0, \tag{39}$$

where the matrix  $U(q)$  encodes the restriction of states with definite momentum and angular momentum to a finite box with cubic geometry. The scattering phase shift  $\delta$  depends on the spin and isospin channels. For the purposes of this paper, the phase shift is written with subscripts as  $\delta_{I\ell}(q)$ , where  $I$  is the isospin and  $\ell$  is the angular momentum. The dimensionless momentum  $\mathbf{q}$  is given by

$$\mathbf{q} = \mathbf{p}L/2\pi. \quad (40)$$

The center-of-mass relative momentum of the two-pion states,  $\mathbf{p}$ , is deduced from the two-pion state energy,

$$\mathbf{p}^2 = \frac{1}{4} (E_{\pi\pi}^2 - (2M_\pi)^2 - \mathbf{P}^2), \quad (41)$$

where the energy  $E_{\pi\pi}$  is fit from lattice data and  $\mathbf{P}$  is the momentum of the center of mass. The matrix  $U(q)$  is related to the scattering matrix  $\mathcal{M}$  by

$$U = (\mathcal{M} + i\mathbb{1})(\mathcal{M} - i\mathbb{1})^{-1}. \quad (42)$$

$\mathcal{M}$  is determined on the lattice from a series of subduction coefficients  $S$ , Wigner  $\mathcal{D}$ -matrices, and a cubic rotation scattering matrix  $M$ , as a function of  $q \propto p$ ,

$$\begin{aligned} \mathcal{M}_{\ell,n;\ell',n'}^{\mathbf{P},\Lambda}(q) &= \frac{1}{\dim\Lambda_{\mathbf{P}}} \sum_{\mu} \sum_{\lambda,\lambda'} \sum_{mm'} \\ &\times S_{\Lambda(n),\mu}^{\mathbf{P},\ell,\lambda} * S_{\Lambda(n'),\mu}^{\mathbf{P},\ell',\lambda'} \\ &\times \mathcal{D}_{m\lambda}^{\ell}(\hat{R}_0) \mathcal{D}_{m'\lambda'}^{\ell'}(\hat{R}_0) \\ &\times M_{\ell,m;\ell',m'}^{\mathbf{P}L/2\pi}(q). \end{aligned} \quad (43)$$

Here,  $\dim\Lambda_{\mathbf{P}}$  is the number of elements of the cubic rotation group irrep  $\Lambda$  that have total center-of-mass momentum  $\mathbf{P}$ . Index  $\mu$  is the ‘‘row’’ of the irrep  $\Lambda$ , and is an element of the irreducible representation vector space. The indices  $\ell^{(\prime)}$  are total angular momentum quantum numbers,  $\lambda^{(\prime)}$  are helicity magnitude quantum numbers, and  $m^{(\prime)}$  are  $z$ -component angular momentum quantum numbers. The indices  $n^{(\prime)}$  are used to denote distinct replicas of the irrep  $\Lambda$  within the decomposition of  $\ell^{(\prime)}$ , since more than one of the same irrep may be obtained from a single angular momentum decomposition.

The matrix  $M$  can then be reduced to a series of Clebsch-Gordan coefficients  $C$  of  $SU(2)$  spin and a known geometric function  $\mathcal{Z}$ ,

$$\begin{aligned} M_{\ell m,\ell' m'}^{\mathbf{d}}(q) &= -i\gamma^{-1} \frac{(-1)^\ell}{\pi^{3/2}} \\ &\times \sum_{j=|\ell-\ell'|}^{\ell+\ell'} \sum_{s=-j}^j (-iq)^{-(j+1)} \mathcal{Z}_{js}^{\mathbf{d}}(1;q) C_{\ell m,j s,\ell' m'}. \end{aligned} \quad (44)$$

The factor  $\gamma$  is the Lorentz contraction factor computed with the momentum  $\mathbf{P}$ .

Although Eq. (43) is written in a manifestly basis-independent form due to the sum over irrep row  $\mu$ , Schur orthogonality relations may be used to prove that the computation with a single irrep row is also basis independent.

## G. Correlated Subtraction of One-Pion States

To improve upon the precision of the extracted spectrum, it is beneficial to exploit the correlation between statistical fluctuations of the one-pion and two-pion correlation functions. The phase shift may be computed using the energy difference between the usual interacting two-pion system and a ‘‘noninteracting’’ two-pion system, where noninteracting here means that the two pions are not allowed to exchange gluons or quarks. This is an improvement over strategies that implement the ratio of correlation functions, such as in Refs. [33–35].

To make this procedure more concrete, consider the one-pion two-point correlation function with definite momentum  $\mathbf{P}_0$ ,

$$C_{\pi,\mathbf{P}_0}(t) = \langle \mathcal{O}_{\pi,\mathbf{P}_0}(t) \mathcal{O}_{\pi,\mathbf{P}_0}^\dagger(0) \rangle. \quad (45)$$

This correlation function will have as its ground state the energy of a pion moving with momentum  $\mathbf{P}_0$ ,  $E_{\pi,\mathbf{P}_0}$ . This is combined in a product with another correlator with momentum  $\mathbf{P}_1$  such that the two correlators form a noninteracting two-pion correlator with total momentum  $\mathbf{P} = \mathbf{P}_0 + \mathbf{P}_1$ ,

$$C_{\pi\pi,\mathbf{P}_0,\mathbf{P}_1}^{\text{NI}}(t) = C_{\pi,\mathbf{P}_0}(t) C_{\pi,\mathbf{P}_1}(t). \quad (46)$$

Since no particles are exchanged, the noninteracting two-pion system only yields nonzero correlation functions when momentum is conserved for each pion independently. Therefore, this correlator will have as its ground state the sum of the two one-pion energies,

$$E_{\pi\pi,\mathbf{P}_0,\mathbf{P}_1}^{\text{NI}} = E_{\pi,\mathbf{P}_0} + E_{\pi,\mathbf{P}_1}. \quad (47)$$

Eq. (46) is then averaged over all momentum combinations that are connected by rotations to optimize the statistical precision while retaining the statistical fluctuations of the interacting two-pion correlators.

In contrast to the noninteracting two-pion correlator, the usual interacting two-pion correlation functions will contain contributions where the pions exchange momentum. This means that the interacting two-pion correlation functions will have a tower of two-pion states. Provided that there is no resonance in the two-pion channel and that the energy is low enough that neither single pion can be promoted to an excited state, the states of the spectrum are in one-to-one correspondence with the noninteracting energy levels. The interacting energy levels may therefore be identified by the momenta of the corresponding noninteracting momenta and so may be written as  $E_{\pi\pi,\mathbf{P}_0,\mathbf{P}_1}$ . Then the interacting-noninteracting energy difference is

$$\Delta E_{\pi\pi,\mathbf{P}_0,\mathbf{P}_1} = E_{\pi\pi,\mathbf{P}_0,\mathbf{P}_1} - E_{\pi\pi,\mathbf{P}_0,\mathbf{P}_1}^{\text{NI}}. \quad (48)$$

For the purposes of evaluating the Lüscher quantization condition, the center-of-mass momentum of the two pion system must be obtained from the relation

$$\mathbf{p}^2 = \frac{1}{4} ((E_{\pi\pi})^2 - (2M_\pi)^2 - \mathbf{P}^2). \quad (49)$$

To leverage the precise energy difference obtained from Eq. (48), the two-pion energy in Eq. (49) is replaced with

$$E_{\pi\pi} \rightarrow E_{\pi,\mathbf{P}_0} + E_{\pi,\mathbf{P}_1} + \Delta E_{\pi\pi,\mathbf{P}_0,\mathbf{P}_1} \quad (50)$$

$$\mathbf{p}^2 = \frac{1}{4} \left( (\Delta E_{\pi\pi,\mathbf{P}_0,\mathbf{P}_1})^2 + 2(\Delta E_{\pi\pi,\mathbf{P}_0,\mathbf{P}_1})(E_{\pi,\mathbf{P}_0} + E_{\pi,\mathbf{P}_1}) + (E_{\pi,\mathbf{P}_0} + E_{\pi,\mathbf{P}_1})^2 - (2M_\pi)^2 - \mathbf{P}^2 \right). \quad (51)$$

The one-pion energies inserted into Eq. (51) may additionally be replaced by their continuum counterpart obtained by applying the dispersion relation to the pion mass,

$$E_{\pi,\mathbf{P}_i} \rightarrow \sqrt{M_\pi^2 + \mathbf{P}_i^2}. \quad (52)$$

This has the added benefit of removing some of the discretization effects that appear in the energy of the moving one-pion state, making the energy difference  $\Delta E_{\pi\pi,\mathbf{P}_0,\mathbf{P}_1}$  the dominant source of discretization errors.

### III. COMPUTATION DETAILS

#### A. Ensemble Details

Ensemble	$L^3 \times T$	$a^{-1}$ [GeV]	# Conf.	# Evcs
24ID	$24^3 \times 64$	1.015(15)	33	120
48I	$48^3 \times 96$	1.730(4)	27	60

TABLE I. Details of the ensembles used in this study. Both ensembles used have physical  $M_\pi$  [36].

This project uses the physical pion mass 2+1 flavor Möbius Domain Wall Fermion gauge configurations generated by the RBC-UKQCD collaboration, labeled as 24ID and 48I. The 48I ensemble uses an Iwasaki gauge action [37], while the 24ID uses the Iwasaki action combined with a Dislocation-Suppressing Determinant Ratio (Iwasaki+DSDR) method [38–41]. The lattice dimensions and lattice spacings are provided in Table I. Both gauge ensembles are generated with physical quark masses, and all Dirac matrix solves are computed with the valence mass equal to the sea light-quark mass.

#### B. Dirac Equation Solutions

The distillation perambulators are computed using eigenvectors of the 3-dimensional Laplacian operator in Eq. (5). The links  $U_i$  in the Laplacian have been Gaussian smeared in both space and time with  $\rho = 0.1$  and  $N = 30$ . Smearing in the time direction is kept ultra-local by zeroing out all but timeslices  $t-1$ ,  $t$ , and  $t+1$ , smearing in all 4 dimensions, and then retaining only timeslice

to obtain

$t$ . This procedure is repeated for every timeslice  $t$  over the entire configuration.<sup>1</sup> The effect of smearing in the time direction smooths out fluctuations in the correlation functions but otherwise does not affect the final precision of measurements.

All measurements obtained on a single configuration are averaged together and treated as a single data sample to avoid correlation between measurements on the same configuration. The sample configurations are separated by enough Markov Chain Monte Carlo trajectories so that no autocorrelation is observed in the correlator data. For this reason, each configuration is treated as independent and no blocking over configurations is performed. Statistical uncertainties on correlation functions and derived quantities are computed using jackknife resampling.

Correlation functions used in this analysis are computed with interpolating operators that couple to  $\pi\pi$  states in the isospin 0 and isospin 2 channels. Distillation operators are constructed with unit weights applied equally to all eigenmodes in the distillation basis. Other interpolating operators may be achieved by relaxing this constraint, but no such study was performed here. All of the  $\pi\pi$  interpolating operators used in this analysis are constructed from two quark bilinears with equal and opposite Fourier phases, corresponding to 0 total center-of-mass momentum. In the isospin 0 channel, an additional distillation-smear scalar current was also included in the basis. No links were used to point split the operators, which could be used to generate operators in nontrivial spin representations.

As a rule of thumb, it is possible to guess how many  $\pi\pi$  states are accessible within statistics based on the number of distillation eigenvectors included in the interpolating operators. In a free theory, the eigenvectors of the Laplacian operator used for the distillation basis are plane waves, with eigenvalues corresponding to the momentum squared. With  $N_v$  eigenvectors, it is then possible to access momenta up to  $P_{\max}$  given by

$$|P_{\max}|^2 \approx (N_v/3)^{\frac{1}{3}}, \quad (53)$$

<sup>1</sup> The source code for generating this smearing can be found online: <https://github.com/lehner/gpt/blob/master/applications/distillation/booster-96I-basis.py>

where the factor of 3 accounts for color dilution and the power of  $1/3$  comes from filling all eigenvector momenta in three spatial directions. From this counting, momenta up to  $|P_{\max}|^2 \approx 3.4$  for the 24ID ensemble and  $|P_{\max}|^2 \approx 2.7$  on the 48I ensemble are expected to be well-constrained by the distillation data. Empirically, momenta up to  $|P_{\max}|^2 = 4$  were found to be precise enough to use in this analysis.

### C. AMA Bias Correction of Correlation Functions

The All Mode Averaging (AMA) [42] bias correction procedure is performed on one-, two-, and three-point correlation functions. Each of these correlation function types have a different set of available timeslices on which to compute the bias correction, so some description of the procedure is in order. On both ensembles, “exact” full-precision solves are computed for all eigenvectors on timeslices in the set  $\mathcal{T}_{\text{exact}} = \{t/a \in \{0, \dots, 15\}\}$ . The low-precision “sloppy” solves are computed on every timeslice of each configuration, i.e.  $\mathcal{T}_{\text{sloppy},24\text{ID}} = \{t/a \in \{0, \dots, 63\}\}$  and  $\mathcal{T}_{\text{sloppy},48\text{I}} = \{t/a \in \{0, \dots, 95\}\}$ .

For the  $1\pi$  two-point and three-point functions, the sink operator consists of a single quark bilinear operator. The valence quark lines propagating outward from the sink operator does not connect the sink timeslice back to itself. As a consequence, the antiquark line may always be obtained using  $\gamma_5$  hermiticity in Eq. (8), thereby avoiding the need for inversions on the sink timeslice. So long as the source operator (and insertion operator for the three-point function) are contained within  $\mathcal{T}_{\text{exact}}$ , a viable full-precision solve may be obtained for the bias correction of the correlation function. Therefore, all sink timeslices for the  $1\pi$  two-point functions and all sink timeslices for  $1\pi$  three-point functions with insertion time  $\tau/a \in \mathcal{T}_{\text{exact}}$ , which is satisfied by all data in this manuscript, may be bias corrected with the AMA procedure.

In  $1\pi$  two-point correlation functions, the bias correction is computed and averaged over all source times before being added to the sloppy solves. For “sloppy” solves  $S$  and “exact” solves  $X$ , the bias correction procedure is written as

$$\begin{aligned} B(t) &= \langle X_{t_0}(t) - S_{t_0}(t) \rangle_{t_0 \in \mathcal{T}_{\text{exact}}}, \\ A(t) &= B(t) + \langle S_{t_0}(t) \rangle_{t_0 \in \mathcal{T}_{\text{sloppy}}}, \end{aligned} \quad (54)$$

where  $A$  and  $B$  denote the full bias-corrected data and the bias correction term, respectively. In this equation,  $t_0$  denotes the source time for equivalent correlators related by time translation. The  $1\pi$  three-point correlation functions are similarly computed, being sure to keep both the source time and insertion time within the allowed ranges:

$$\begin{aligned} B(t, \tau) &= \langle X_{t_0}(t, \tau) - S_{t_0}(t, \tau) \rangle_{\{t_0, t_0 + \tau\} \in \mathcal{T}_{\text{exact}}}, \\ A(t, \tau) &= B(t, \tau) + \langle S_{t_0}(t, \tau) \rangle_{\{t_0, t_0 + \tau\} \in \mathcal{T}_{\text{sloppy}}}. \end{aligned} \quad (55)$$

In contrast with the  $1\pi$  correlation functions, the  $\pi\pi$  interpolating operators used in this analysis require solutions to the Dirac equation originating from both the source and sink timeslices. The bias correction may therefore only be applied to timeslices where it is possible to construct both of the  $\pi\pi$  interpolating operators on timeslices within the set  $\mathcal{T}_{\text{exact}}$ . When these correlators are substituted into the GEVP equation, the range of available bias correction data is reduced further. For larger time separations, only the average of the sloppy measurements is available, which could introduce a bias in the result. The data out beyond the region where the AMA bias correction is available is used only for checking consistency and to demonstrate general trends of the data beyond the available time range.

The bias-correction procedure for the  $\pi\pi$  two-point correlation functions may then be written

$$\begin{aligned} B(t) &= \langle X_{t_0}(t) - S_{t_0}(t) \rangle_{\{t_0, t_0 + t\} \in \mathcal{T}_{\text{exact}}}, \\ A(t) &= B(t) + \langle S_{t_0}(t) \rangle_{\{t_0, t_0 + t\} \in \mathcal{T}_{\text{sloppy}}}. \end{aligned} \quad (56)$$

This equation is applicable for the isospin 2 channel  $\pi\pi$  correlation functions, even with thermal corrections applied as in Eq. (33).

The only remaining bias correction to discuss is the isospin 0 channel with the additional vacuum subtraction, as detailed in Eqs. (36)–(38). This is made more complicated by the correlation of source times between the one-point function and the two-point function. The correct way to perform this subtraction is to apply Eq. (56) to the vacuum-subtracted correlation function in Eq. (37). This ensures that both timeslices in the product of one-point functions are contained within  $\mathcal{T}_{\text{exact}}$  when the bias correction is performed. After the correlation function is bias-corrected, the remaining thermal subtraction in Eq. (38) may be performed on the corrected correlators.

## IV. SPECTRUM ANALYSIS

### A. Corrections to Two-Point Correlation Functions

As discussed in Sec. IID, the  $\pi\pi$  correlation functions have significant contributions from thermal contaminations due to  $1\pi$  states that propagate through the periodic temporal boundary. These manifest as exponential correlator contributions with small energies that are exponentially suppressed by the lattice temporal extent. If not properly removed, these terms could cause the spectrum to be underestimated or fail to reach a plateau.

The temporal contributions in this analysis are removed by computing them in a dedicated calculation and subtracting them from the  $\pi\pi$  correlators. This is accomplished in two steps. The first step is to compute the spectrum and matrix elements for one-pion (denoted  $1\pi$ ) two-point correlation functions for each lattice momentum. The second step is to insert a  $\pi\pi$  operator between

two  $1\pi$  interpolating operators to compute a three-point function. Using the spectrum and matrix elements from the first step, the three-point function is used to compute a transition matrix element that connects a  $1\pi$  state back to itself.

### 1. One-Pion Fits

For the first step in the process, the  $1\pi$  two-point correlation functions are computed to extract the spectrum and matrix elements for the distillation-smear pseudoscalar source and sink operators. These correspond to the expectation values

$$\begin{aligned} & \langle \mathcal{O}_{\pi, \mathbf{p}_\pi}(t) \mathcal{O}_{\pi, \mathbf{p}_\pi}^\dagger(0) \rangle \\ &= \sum_m^\infty \langle 0 | \mathcal{O}_{\pi, \mathbf{p}_\pi} | \pi^0 \rangle_m \langle \pi^0 | \mathcal{O}_{\pi, \mathbf{p}_\pi}^\dagger | 0 \rangle e^{-E_{\pi, m} t} \\ &+ \sum_m^\infty \langle \pi^0 | \mathcal{O}_{\pi, \mathbf{p}_\pi} | 0 \rangle \langle 0 | \mathcal{O}_{\pi, \mathbf{p}_\pi}^\dagger | \pi^0 \rangle_m e^{-E_{\pi, m}(T-t)}. \end{aligned} \quad (57)$$

The pion states are given a superscript to indicate that they are computed for the neutral pion. The first and second terms of the RHS are the forward- and backward-propagating contributions, respectively, with  $T$  being the total time extent of the lattice.

The  $1\pi$  two-point correlation functions are fit to the sum of exponentials in Eq. (57) using a correlated  $\chi^2$  test statistic. The fit ansatz assumes that the sum is truncated to at most two states  $|\pi^0\rangle_m$ , corresponding to the pion ground state and a single excited state, both with momentum  $\mathbf{p}_{\text{in}} = \mathbf{p}_{\text{out}} \equiv \mathbf{p}_\pi$ . The fits included all data in a range between  $t_{\text{min}}$  and  $t_{\text{max}}$ , with a separate choice of  $t_{\text{min}}$  and  $t_{\text{max}}$  for both 1-state and 2-state fits. The difference between the 1-state and 2-state fits was used as a systematic uncertainty for the contamination due to excited states.

The results of the fits are given in Tables II and III for the 24ID and 48I ensembles, respectively. All the fits on the 24ID ensemble were performed with  $(t_{\text{min}}, t_{\text{max}}) = (3, 14)$  for the 2-state fits and  $(t_{\text{min}}, t_{\text{max}}) = (6, 14)$  for the 1-state fits, corresponding to 7 and 6 degrees of freedom, respectively. Similarly, the 48I ensemble were performed with  $(t_{\text{min}}, t_{\text{max}}) = (5, 16)$  for the 2-state fits and  $(t_{\text{min}}, t_{\text{max}}) = (10, 16)$  for the 1-state fits, corresponding to 7 and 4 degrees of freedom, respectively. These fit

ranges are small enough that the covariance matrix is well-conditioned.

### 2. Pion Transition Matrix Elements

The matrix elements that appear as contamination of the two-point function in Eq. (26) are squares of the  $1\pi$ -to- $1\pi$  matrix elements times an exponential suppression factor. These contributions are observed to be at most at the 1% level, so the precision requirements on these

$\left(\frac{\mathbf{p}L}{2\pi}\right)^2$	$aE_\pi(\text{stat})(\text{syst})$	$\langle 0   \mathcal{O}_\pi   \pi^0 \rangle (\text{stat})(\text{syst})$	$p\text{-val}$
0	0.14015(32)(00)	0.24643(61)(03)	0.950
1	0.29590(48)(10)	0.12878(31)(03)	0.656
2	0.39491(94)(30)	0.09100(26)(13)	0.019
3	0.4748(20)(03)	0.06792(34)(09)	0.573
4	0.5330(42)(14)	0.05104(65)(19)	0.392

TABLE II. Pion masses and matrix elements from  $1\pi$  two-point function fits on the 24ID ensemble. The first column denotes the squared magnitude of the lattice momentum, in units of  $(2\pi/L)^2$ . For each momentum, the mass and matrix elements of the ground state, in lattice units, and the  $p$ -value for the 2-state fit are given. Both statistical and systematic uncertainties are listed, with the only systematic arising from the difference between the 1-state and 2-state fits. The 2-state fits all have 7 degrees of freedom.

$\left(\frac{\mathbf{p}L}{2\pi}\right)^2$	$aE_\pi(\text{stat})(\text{syst})$	$\langle 0   \mathcal{O}_\pi   \pi^0 \rangle (\text{stat})(\text{syst})$	$p\text{-val}$
0	0.08027(20)(06)	0.04841(11)(02)	0.388
1	0.15358(37)(19)	0.021413(48)(71)	0.540
2	0.20320(38)(29)	0.013060(35)(30)	0.383
3	0.2408(09)(08)	0.008396(36)(44)	0.519
4	0.2743(19)(29)	0.00558(05)(09)	0.762

TABLE III. The same as Table II, but for the 48I ensemble. Like the 24ID fits, the 2-state fits all have 7 degrees of freedom.

matrix elements is not as great as on the  $\pi\pi$  two-point functions themselves. For this reason, a simplified analysis method is sufficient for extracting the  $1\pi$ -to- $1\pi$  transition matrix elements.

The transition matrix elements needed to complete the subtraction are obtained from a ratio,

$$\langle \pi^0 | \mathcal{O}_X | \pi^0 \rangle \stackrel{t, \tau \rightarrow \infty}{\approx} \sqrt{\frac{\langle \mathcal{O}_{\pi, \mathbf{p}_\pi}(t) \mathcal{O}_X(\tau) \mathcal{O}_{\pi, \mathbf{p}_\pi}^\dagger(0) \rangle \langle \mathcal{O}_{\pi, \mathbf{p}_\pi}(t) \mathcal{O}_X(t-\tau) \mathcal{O}_{\pi, \mathbf{p}_\pi}^\dagger(0) \rangle}{\langle \mathcal{O}_{\pi, \mathbf{p}_\pi}(t) \mathcal{O}_{\pi, \mathbf{p}_\pi}^\dagger(0) \rangle \langle \mathcal{O}_{\pi, \mathbf{p}_\pi}(t) \mathcal{O}_{\pi, \mathbf{p}_\pi}^\dagger(0) \rangle}} \equiv R(t, \tau). \quad (58)$$

Here,  $\mathcal{O}_X$  is a stand-in for either the distillation-smear scalar operator  $\mathcal{O}_1$  in Eq. (17) or the  $\pi\pi$  op-

erators  $\mathcal{O}_{\pi\pi}\left(\left|\frac{\mathbf{p}_{\text{rel}}L}{2\pi}\right|^2\right)$  with back-to-back momenta  $\mathbf{p}_{\text{rel}}$

in Eq. (19). The scalar operator is only permitted in the isospin 0 channel. The pion operators  $\mathcal{O}_{\pi, \mathbf{p}_\pi}$  are constructed with momentum  $\mathbf{p}_\pi$ , to give the ingoing and outgoing  $1\pi$  states momentum. The times  $t$  and  $\tau$  correspond to the source-sink and source-insertion times, respectively. Data for the three-point functions are generated for source-insertion times  $\tau/a \in \{3, 6, 9, 12\}$ , and source-sink separation times up to  $t/a = 24$ . The correlators are computed for all of the  $\pi\pi$  and scalar operators that are included in the analysis of  $\pi\pi$  two-point function analysis and for ingoing/outgoing momenta  $|\mathbf{p}_\pi L/2\pi|^2 \leq 4$ .

Symmetrizing over the three-point function times in the numerator of Eq. (58) helps by canceling the exponential falloff of the numerator and denominator. This ratio assumes that the correlation functions in the numerator and the denominator have only one state contributing to the correlation function. While this will not be strictly true, the correlation function does indeed appear to be dominated by the ground state. The excited state pion has a mass of  $\sim 1300$  GeV [43], indicating that it is expected to be highly suppressed compared to the single, unexcited pion state.

For many of the choices of operator and momenta, this ratio exhibits a distinct dependence on the source-sink time  $t$  as  $t$  becomes large, as seen for the blue circles plotted in Fig. 1. This is due to the backward-propagating pion term in the correlation function in Eq. (57), which contributes nonnegligibly to the denominator of Eq. (58). To correct for this, the  $1\pi$  two-point correlation functions in the denominator of Eq. (58) are replaced by only the forward-propagating exponential from the  $1\pi$  ground state obtained from fits in the previous section,

$$\langle \mathcal{O}_\pi(t) \mathcal{O}_\pi^\dagger(0) \rangle \rightarrow |\langle 0 | \mathcal{O}_\pi | \pi^0 \rangle|^2 e^{-E_\pi t}. \quad (59)$$

The ratio using only the forward-propagating exponential is plotted in Fig. 1 using various symbols and colors, versus the ratio with the unmodified two-point correlator shown as blue circles. After correcting for the backward-propagating term in the denominator, all of the ratio data for various  $t/a$  and  $\tau/a$  are consistent with each other within uncertainties. This agreement is seen for all choices of operators and momentum in the isospin 2 channel, with the exception of only the smallest  $\tau/a$  on the 48I ensemble where excited state contamination is visible.

In addition to the backward propagating pion in the denominator of the ratio of Eq. (58), the numerator of the isospin 0 three-point functions also exhibit a significant contribution from a backward-propagating pion. This contamination is due to a vacuum matrix element that is not present in the isospin 2 channel,

$$\begin{aligned} & \langle \mathcal{O}_\pi(t) \mathcal{O}_X(\tau) \mathcal{O}_\pi^\dagger(0) \rangle \\ & \approx \langle 0 | \mathcal{O}_\pi | \pi^0 \rangle \langle \pi^0 | \mathcal{O}_X | \pi^0 \rangle \langle \pi^0 | \mathcal{O}_\pi^\dagger | 0 \rangle e^{-E_\pi t} \\ & + \langle \pi^0 | \mathcal{O}_\pi | 0 \rangle \langle 0 | \mathcal{O}_X | 0 \rangle \langle 0 | \mathcal{O}_\pi^\dagger | \pi^0 \rangle e^{-E_\pi(T-t)}. \end{aligned} \quad (60)$$

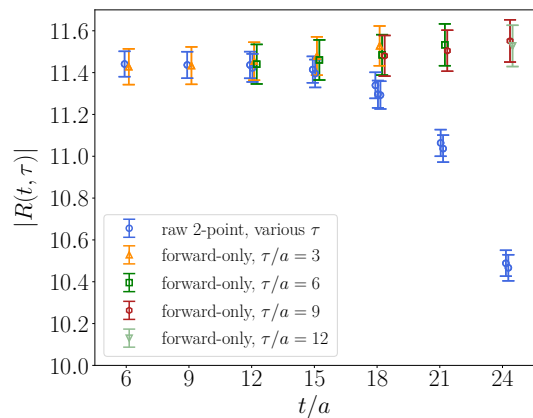


FIG. 1. Transition matrix element for the three-point correlation function in the isospin 2 channel on the 24ID ensemble, where the effect of changing the denominator is most prominent. The ratio  $|R(t, \tau)|$  for this plot asymptotes to  $\langle \pi^0 | \mathcal{O}_{\pi\pi}(0) | \pi^0 \rangle$  with ingoing and outgoing pion momentum  $\mathbf{p}_\pi = 0$ . The data labeled “raw 2-point” use the raw correlation function in the denominator of  $R(t, \tau)$  given in Eq. (58). The “forward-only” data include only the forward-propagating exponential in the denominator, as described by Eq. (59). For the “forward-only” ratio data, values with distinct  $\tau$  are plotted with separate symbols and colors.

For all but the lightest pion state, these contributions are safely negligible. However, the pion at rest propagating through the temporal boundary condition has a small enough mass to contribute nonnegligibly. These contributions are estimated using the vacuum matrix elements approximated by the raw one-point correlation function,

$$\langle 0 | \mathcal{O}_X | 0 \rangle \approx \langle \mathcal{O}_X \rangle, \quad (61)$$

and the overlaps and energies computed from the  $1\pi$  two-point correlation functions. The three-point correlation functions in the numerator are then replaced by the subtracted correlator,

$$\begin{aligned} & \langle \mathcal{O}_\pi(t) \mathcal{O}_X(\tau) \mathcal{O}_\pi^\dagger(0) \rangle \rightarrow \\ & \langle \mathcal{O}_\pi(t) \mathcal{O}_X(\tau) \mathcal{O}_\pi^\dagger(0) \rangle - \langle \mathcal{O}_X \rangle |\langle 0 | \mathcal{O}_\pi | \pi^0 \rangle|^2 e^{-E_\pi(T-t)}. \end{aligned} \quad (62)$$

The ratio data using the raw three-point correlation functions and the ratios after the subtraction of Eq. (62) are plotted in Fig. 2. In this figure, the ratio data without the subtraction exhibit a definitive upward trend with increasing  $t/a$  due to the backward-propagating one-pion state with the vacuum contribution. This trend vanishes after the subtraction and all data are very consistent over the entire set of times plotted. After performing the subtractions of the backward-propagating one-pion state in both the numerator and denominator, the isospin 0 ratio data for all operators and momenta are in good agreement within their quoted uncertainties except for the smallest choice of  $\tau/a$  on the 48I ensemble.

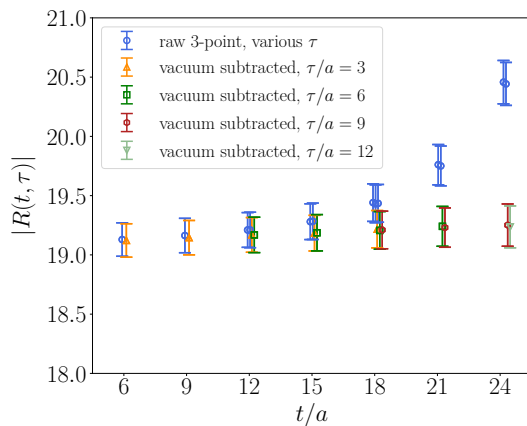


FIG. 2. Transition matrix element for the three-point correlation function in the isospin 0 channel on the 24ID ensemble, where the effect of changing the numerator is most prominent. The ratio  $|R(t, \tau)|$  for this plot asymptotes to  $\langle \pi^0 | \mathcal{O}_{\pi\pi}(0) | \pi^0 \rangle$  with ingoing and outgoing pion momentum  $\mathbf{p}_\pi = 0$ . The data labeled “raw 3-point” use the raw correlation function in the numerator of  $|R(t, \tau)|$  given in Eq. (58). The “vacuum subtracted” data include the subtraction of the term proportional to the vacuum matrix element in the numerator, as described by Eq. (62). All data plotted here have the backward-propagating term removed from the denominator, as described in Eq. (59). For the “vacuum subtracted” ratio data, values with distinct  $\tau$  are plotted with separate symbols and colors.

The ratio values  $R(18, 9)$  for all choices of momentum and isospin are taken as the nominal value for the transition matrix elements. To account for the remaining time dependence due to neglected contaminations from excited states, a systematic uncertainty is included corresponding to the difference  $\delta R = R(18, 9) - R(12, 6)$ .

A summary of the transition matrix elements obtained from the ratio in Eq. (58) with the replacements of the denominator from Eq. (59) and, for the isospin 0 channel, the numerator from Eq. (62) are depicted in Fig. 3 and their values listed in Tables IV–VII. The isospin 0 transition matrix elements, depicted in the top row of Fig. 3, are more agnostic in regards to how strongly the operators couple to any given state compared to the isospin 2 channel. The isospin 2 matrix elements, in the bottom row, exhibit significant suppression of operator-state combinations where  $\mathbf{p}_\pi \neq \mathbf{p}_{\text{rel}}$ . In all cases, the thermal terms associated with these matrix elements will also be suppressed by exponentials of size  $e^{-E_{\mathbf{p}_\pi} T}$ . The only terms that produce a nonnegligible contribution to the correlation function are those with  $\mathbf{p}_{\text{rel}} = (0, 0, 0)$ , which are the left-most (blue) bar for each operator choice.

### 3. Vacuum Matrix Elements

For the isospin 0 channel, the vacuum matrix element terms that appear in Eq. (34) must be accounted for and

subtracted. Since these terms couple only to the vacuum, they have no time dependence and appear as a constant term. These terms can be exactly cancelled from combinations like a simple nearest-neighbor subtraction, Eq. (31), but at the cost of additional statistical noise. Instead, this analysis uses an explicit computation of the  $1\pi$  one-, two-, and three-point correlation functions to reconstruct and subtract the vacuum matrix elements, as outlined in Eqs. (36)–(38).

Care must be taken to account for possible thermal terms in the vacuum contribution. The one-point correlation function in Eq. (35) in a finite temporal volume may be expanded in terms of a complete set of eigenstates, which yields a small, exponentially suppressed thermal contribution to the vacuum matrix element of interest. Assuming the one-point function amplitude is dominated by the vacuum matrix element, the size of the thermal contribution may be estimated from the transition matrix elements computed in the ratio of Eq. (58) by comparing the uncertainty to the total ratio

$$\delta \langle \mathcal{O}_X \rangle \sim 3 \sum_p \langle \pi^0 | \mathcal{O}_X | \pi^0 \rangle e^{-E_\pi T}. \quad (63)$$

In this equation, the factor of 3 is an isospin factor that is described in the discussion around Eq. (30).

The one-point correlation function data and the corresponding thermal contamination for the 0-momentum ingoing and outgoing  $1\pi$  states are listed in Table VIII. For most of the thermal terms, the exponent mass  $E_n$  is large enough that the exponential completely suppresses the contribution. For the 0-momentum pion, however, the term is still comparable to the uncertainty on the one-point correlation function. While the thermal correction to the vacuum matrix element is completely negligible for the 24ID ensemble, the thermal contamination can be as large as the statistical uncertainty for the 48I ensemble. After performing correlated subtraction of the vacuum terms from the  $\pi\pi$  two-point functions, the statistical uncertainty is reduced and the effect of the additional thermal contribution becomes significantly more problematic. For the correlation function with  $\mathbf{p}_\pi = \mathbf{p}_{\text{rel}} = 0$ , subtraction of this additional thermal term results in a correction of about 3.2% on the correlation function at  $t/a = 10$ , while the uncertainty is at the level of 0.8%.

The contribution of the thermal correction to the vacuum matrix element is removed using the one-pion transition matrix elements from Sec. IID, estimated with the ratio in Eq. (58). Both of the corrections in Eqs. (59) and (62) are applied to the transition matrix elements. The corrected vacuum matrix element is then given by Eq. (36), where the  $\mathbf{p}_\pi = 0$  pion thermal contribution is subtracted away.

Though the subtraction schemes for the vacuum matrix elements and the one-pion transition matrix elements both depend on each other, any thermal correction to the vacuum matrix element in Eq. (62) is neglected. This correction on the correction would be proportional to  $e^{-E_\pi(2T-t)}$ , which would make it doubly-suppressed in

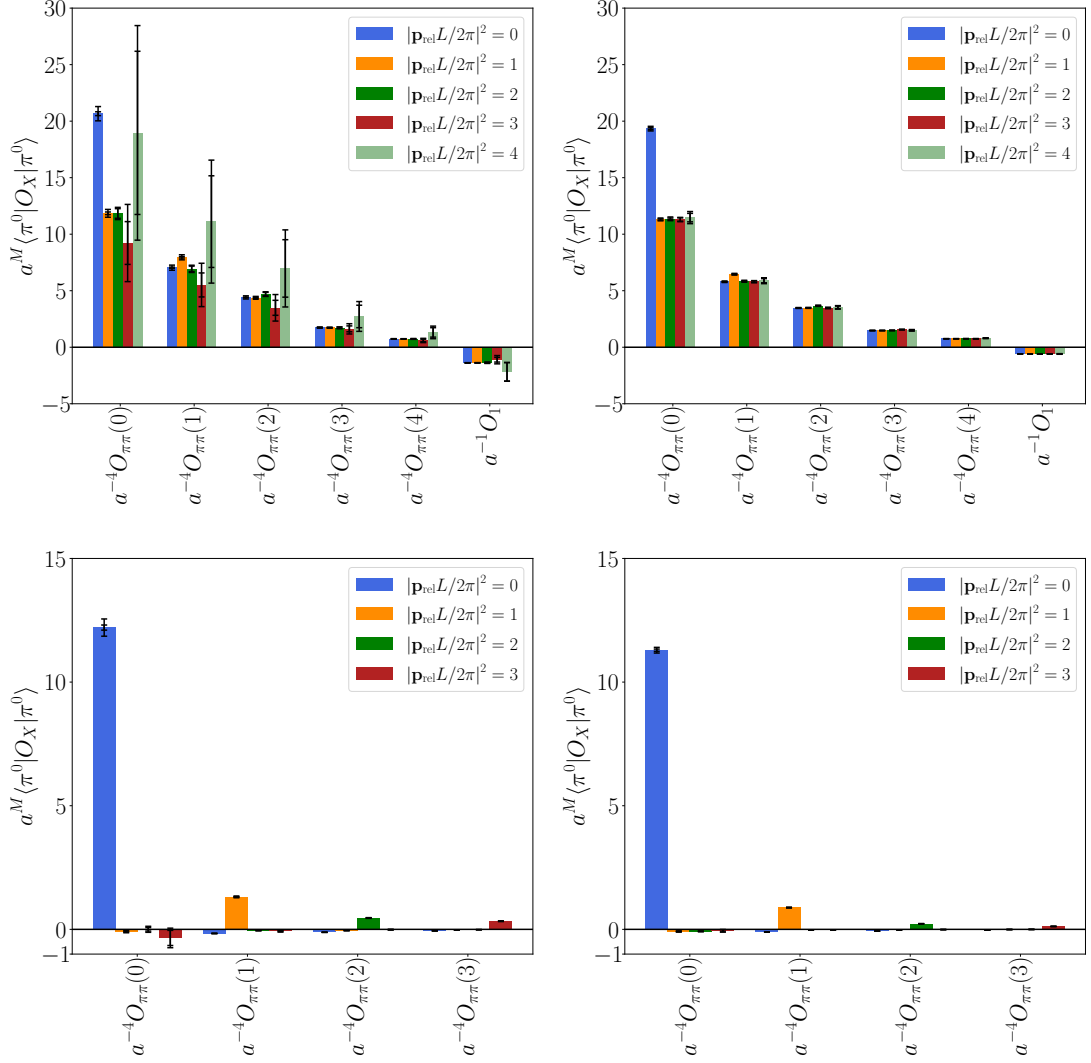


FIG. 3. Summary plots of the size of the  $1\pi$  transition matrix elements,  $a^{-4}\langle\pi^0|\mathcal{O}_{\pi\pi}|\pi^0\rangle$  and  $a^{-1}\langle\pi^0|\mathcal{O}_1|\pi^0\rangle$ , over all choices of external pion momentum  $\mathbf{p}_{\text{rel}}$  (bar color) and over the operator construction (horizontal axis displacement). The  $\pi\pi$  operators are labeled by the values of  $|\mathbf{p}_{\text{rel}}L/2\pi|^2$  for the bilinears that make up the operator (in parentheses). The top (bottom) row contains the  $I = 0$  ( $I = 2$ ) results. For the isospin 0 channel, the scalar operator from Eq. (17) is also included. The left column contains results for the 24ID ensemble, and the right column for 48I ensemble. Both statistical and total uncertainties are plotted.

$\mathbf{p}_\pi$	$\mathbf{p}_{\text{rel}}$	$\langle\pi^0 \mathcal{O}_X \pi^0\rangle(\text{stat})(\text{syst})$					
		(0,0,0)	(1,0,0)	(1,1,0)	(1,1,1)	(2,0,0)	scalar
(0,0,0)		19.43(16)(22)	6.62(05)(10)	4.146(30)(63)	1.636(13)(24)	0.694(07)(10)	-1.361(09)(14)
(1,0,0)		11.14(11)(05)	7.484(61)(13)	4.113(38)(06)	1.625(15)(02)	0.6915(72)(10)	-1.359(12)(03)
(1,1,0)		11.13(40)(10)	6.52(22)(10)	4.42(14)(05)	1.619(56)(22)	0.690(24)(09)	-1.354(47)(27)
(1,1,1)		8.7(1.8)(2.7)	5.2(1.0)(1.5)	3.3(0.6)(0.9)	1.53(25)(35)	0.56(10)(14)	-1.09(21)(30)
(2,0,0)		17.8(6.8)(5.8)	10.5(3.8)(3.4)	6.6(2.4)(2.1)	2.6(0.9)(0.8)	1.23(39)(34)	-2.14(80)(17)

TABLE IV. Table of  $1\pi$  transition matrix elements for the 24ID ensemble in the isospin 0 channel. The momenta  $\mathbf{p}_\pi$  and  $\mathbf{p}_{\text{rel}}$  are defined in Eqs. (32) and (19), respectively. The matrix elements reported here are obtained from the ratio in Eq. (58). The systematic uncertainty comes from the fits to  $1\pi$  two-point correlation functions and from the difference of ratio times.

the temporal extent of the lattice. An improperly estimated vacuum matrix element would express itself as a

$\mathbf{p}_\pi$	$\mathbf{p}_{\text{rel}}$	$\langle \pi^0   \mathcal{O}_X   \pi^0 \rangle (\text{stat})(\text{syst})$					
		(0,0,0)	(1,0,0)	(1,1,0)	(1,1,1)	(2,0,0)	scalar
(0,0,0)		2.159(08)(07)	0.6467(27)(34)	0.3876(18)(17)	0.1649(09)(07)	0.08408(49)(33)	-0.3379(09)(08)
(1,0,0)		1.2622(63)(44)	0.7212(40)(27)	0.3884(24)(13)	0.1650(11)(06)	0.08396(63)(29)	-0.3398(15)(11)
(1,1,0)		1.268(08)(12)	0.6519(44)(55)	0.4093(30)(27)	0.1658(13)(13)	0.08436(72)(64)	-0.3418(18)(21)
(1,1,1)		1.261(16)(07)	0.6476(78)(34)	0.3878(47)(19)	0.1743(21)(08)	0.0838(11)(04)	-0.3394(39)(18)
(2,0,0)		1.280(42)(41)	0.657(21)(20)	0.394(12)(12)	0.1673(53)(50)	0.0898(28)(23)	-0.344(11)(12)

TABLE V. Same as Table IV, but for the 48I ensemble.

$\mathbf{p}_\pi$	$\mathbf{p}_{\text{rel}}$	$\langle \pi^0   \mathcal{O}_{\pi\pi}   \pi^0 \rangle (\text{stat})(\text{syst})$				
		(0,0,0)	(1,0,0)	(1,1,0)	(1,1,1)	(2,0,0)
(0,0,0)		11.48(10)(04)	-0.1563(17)(03)	-0.1125(11)(04)	-0.05489(58)(21)	-0.03071(35)(11)
(1,0,0)		-0.083(17)(43)	1.2352(61)(24)	-0.04440(53)(16)	-0.01986(26)(03)	-0.01049(17)(11)
(1,1,0)		0.00(07)(09)	-0.0445(44)(18)	0.4330(40)(42)	-0.0112(09)(14)	-0.00645(49)(26)
(1,1,1)		-0.33(29)(23)	-0.067(17)(32)	-0.012(08)(10)	0.3100(46)(70)	-0.0025(22)(14)

TABLE VI. Same as Table IV, but for the isospin 2 channel.

$\mathbf{p}_\pi$	$\mathbf{p}_{\text{rel}}$	$\langle \pi^0   \mathcal{O}_{\pi\pi}   \pi^0 \rangle (\text{stat})(\text{syst})$				
		(0,0,0)	(1,0,0)	(1,1,0)	(1,1,1)	(2,0,0)
(0,0,0)		1.2603(51)(14)	-0.01221(09)(11)	-0.008082(52)(03)	-0.003408(38)(02)	-0.001609(21)(02)
(1,0,0)		-0.0096(05)(28)	0.0983(06)(14)	-0.002313(26)(25)	-0.000730(09)(08)	-0.0002245(66)(43)
(1,1,0)		-0.0092(08)(12)	-0.00283(09)(23)	0.02545(17)(55)	-0.000339(12)(03)	-0.0000724(53)(54)
(1,1,1)		-0.0065(51)(24)	-0.00220(22)(04)	-0.000923(67)(20)	0.01326(12)(54)	-0.000068(16)(19)

TABLE VII. Same as Table VI, but for the 48I ensemble.

residual time dependence of the ratio that grows with  $t/a$ , which could be seen in, for example, Fig. 2. No evidence of these neglected contributions is visible.

## B. Two-pion Spectrum Results

The spectrum of states for the  $\pi\pi$  two-point correlation functions is determined from the GEVP using a basis of operators constructed using the distillation smearing. For the isospin 0 and isospin 2 channels in the rest frame,  $\pi\pi$  operators may be constructed with back-to-back momenta of magnitude  $|\mathbf{p}_{\text{rel}}L/2\pi|^2 \in \{0, 1, 2, 3, 4\}$ . In addition, the isospin 0 channel includes a distillation-smear scalar current bilinear operator.

Before the spectrum is computed, subtraction schemes are applied to the correlation function to remove nuisance terms. These subtractions are described in detail in Sec. II. There are the two terms that are the target of the subtractions; first are the thermal terms discussed in Sec. IID, and the second are the vacuum terms discussed in Sec. IIE. Details about the computation of the matrix elements needed to construct the subtraction terms are given in Sec. IVA.

The effects of various subtraction schemes are plotted in Fig. 4. To construct this plot, the GEVP eigenvalues are converted to energies by inverting the formula in

Eq. (24) assuming  $m = n$ ,

$$aE_n(t_0, \delta t) = -\frac{1}{\delta t/a} \log \Lambda_{nn}(t_0, t_0 + \delta t). \quad (64)$$

The effective energies from Eq. (64) are computed and the difference with a fixed timeslice,

$$\Delta aE_n(t_0, \delta t) = aE_n(t_0, \delta t) - aE_n(\bar{t}_0, \delta t) \quad (65)$$

with  $\bar{t}_0$  and  $\delta t$  held fixed. In Fig. 4,  $\bar{t}_0/a = 11$  for both choices of isospin. This energy difference is applied to reduce the difference between the sloppy-only and bias-corrected results so stability over an extended time range can be demonstrated. Because of this subtraction, the plateaux for various subtraction schemes are not required to be in agreement with each other. The isospin 0 channel is plotted on the left side of Fig. 4, and the isospin 2 channel is plotted on the right side.

In Fig. 4, the “unmodified” correlator is the spectrum obtained from the raw data for the  $\pi\pi$  two-point correlation functions. “Thermal subtraction” corresponds to the subtraction of  $1\pi$  state contributions that propagate through the temporal time extent, written in Eq. (33). “Thermal+vacuum subtraction” additionally removes the terms from the isospin 0 channel that have no propagating states, written in Eqs. (37) and (38) and neglecting the thermal correction to the vacuum term by

		$\langle \mathcal{O}_X \rangle$ (stat)					
Ens	$\mathbf{p}_{\text{rel}}$	(0,0,0)	(1,0,0)	(1,1,0)	(1,1,1)	(2,0,0)	scalar
24ID		11.358(58)	6.644(29)	4.162(20)	1.6475(94)	0.7033(52)	-1.3806(49)
48I		1.2775(48)	0.6527(28)	0.3910(19)	0.16625(92)	0.08464(52)	-0.34212(89)
		$10^3 \times 3 \langle \pi^0   \mathcal{O}_X   \pi^0 \rangle e^{-E_\pi T}$ (stat)(syst)					
Ens	$\mathbf{p}_{\text{rel}}$	(0,0,0)	(1,0,0)	(1,1,0)	(1,1,1)	(2,0,0)	scalar
24ID		7.42(16)(09)	2.527(54)(40)	1.583(34)(24)	0.624(14)(09)	0.2648(60)(40)	-0.519(11)(05)
48I		2.915(57)(18)	0.873(16)(06)	0.523(10)(04)	0.2227(42)(15)	0.1135(21)(07)	-0.4561(87)(26)

TABLE VIII. Values of one-point correlation functions (upper) averaged over all timeslices and their corresponding thermal corrections, scaled by a factor of  $10^3$  (lower) on both ensembles. The factor of 3 on the matrix element is a isospin counting factor that is described in the text. These values are strongly correlated timeslice-by-timeslice with the  $\pi\pi$  two-point correlation functions, so the statistical precision of the subtracted two-point correlation function can be smaller than the statistical uncertainty here.

assuming  $C_{\text{vac}} = \langle \mathcal{O}_X \rangle$ . “Thermal+corrected vacuum” applies all of the corrections in Eqs. (36)–(38) as written.

The “time series subtraction” method is the commonly employed strategy for removing contaminants. This strategy applies the modification from Eq. (31) to the matrix of correlation functions before they are substituted into the GEVP. This strategy exactly removes terms that are constant with time, which for correlation functions with 0 total center-of-mass momentum includes all of the thermal and vacuum corrections that appear in both the isospin 0 and 2 channels. The difference is a discrete derivative with respect to Euclidean time, which pulls out an energy-dependent prefactor for the contributions of all of the states. As a result, the effects of excited state contamination at larger Euclidean times are expected to be enhanced from the time series subtraction scheme.

In the isospin 2 channel, the “unmodified” data is expected to have a contamination in the ground state from the thermal terms. This correction is a small constant term in the correlation function that prevents the ground state effective energy from plateauing, which is clearly seen at late times. The “thermal subtraction” removes the thermal terms by applying the subtraction of Eq. (33), which removes the visible contamination. The “time series subtraction,” Eq. (31) with  $dt = 3$ , is also provided as a reference point. The thermal subtraction is used as the nominal choice for the isospin 2 channel, and will be referred to as the “matrix element subtraction” method for isospin 2 in the remainder of the manuscript.

In the isospin 0 channel, the same patterns are seen as in the isospin 2 channel. The “unmodified” data still exhibit a contamination from thermal effects, which produces effective energies that never reach a plateau at large times. This contaminant is removed by applying the “thermal subtraction” of Eq. (33). The thermal subtraction still retains an effective energy consistent with 0, which absorbs all of the contamination from the vacuum term, so no slow falloff of the effective energy is observed. The “thermal+vacuum subtraction” removes most of the vacuum contribution, but reintroduces thermal effects that again prevent a plateau at large time,

similar to the “unmodified” data. Correction of the vacuum term, shown as “thermal+corrected vacuum,” removes the new thermal effects and restores the plateau behavior that is seen in the “thermal subtraction” but without the additional vacuum state in the GEVP. The “time series subtraction” method is again shown for reference with the other subtraction schemes, with  $dt = 3$ . The “thermal+corrected vacuum” is used as the nominal choice, for the isospin 0 channel in the remainder of the manuscript, referred to as the “matrix element subtraction” for isospin 0 from this point on.

Plots of the spectrum obtained from the GEVP as a function of  $t_0$  for both the matrix element subtraction and the time series subtraction schemes are shown in Fig. 5. The plotted data are the energy levels inferred from the eigenvalues after solving the GEVP equation (64). For each jackknife sample, the eigenvalues are sorted so that they optimize Eq. (25) with  $t' = t - 1$  for  $t > 3$ . In the top row of plots,  $\delta t$  is held fixed and  $t_0$  is varied along the horizontal axis. The bottom row shows instead with  $t_0$  fixed and  $\delta t$  varied. For the isospin 2 channel, the thermal contributions have been subtracted away. For the isospin 0 channel, both the (corrected) vacuum and thermal contributions have been subtracted.

For the isospin 2 channel, the states are well-separated over the entire range of  $t_0$  and  $\delta t$  studied for the 48I. The 24ID ensemble exhibits a similar pattern for all states in the isospin 2 channel and up to and including the second excited state in the isospin 0 channel, although the precision for the highest excited states starts to degrade for times  $t_0 \gtrsim 8$ .

For the isospin 0 channel on the 48I ensemble, a spurious state appears in the spectrum at small Euclidean times between the first and second excited states. This spurious state is particularly noticeable in Fig. 5 for the state labeled  $aE_2$  (green squares) in the range  $t_0/a \in \{6, 7, 8\}$ . At  $t_0/a = 8$ , a partial level crossing takes place that causes a degeneracy between  $aE_1$  and  $aE_2$ , spoiling the identification of the state and producing overlapping error bands. For  $t_0/a \geq 9$ , the spurious state effective energy becomes undefined and the second excited state

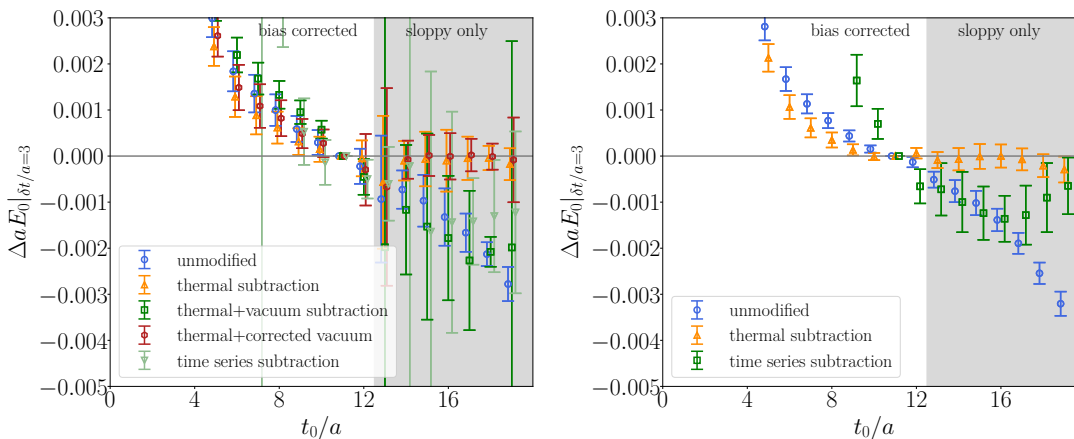


FIG. 4. Comparison of different subtraction schemes. Both plots are on the 48I ensemble; the left plot shows the first  $\pi\pi$  state obtained from the GEVP in the isospin 0 channel, and the right plot shows the ground state for the I=2. The horizontal axis is the correlator time  $t_0$ , and both plots are shown with fixed  $\delta t = 3$ . The vertical axis is the energy difference in lattice units implied from the GEVP eigenvalue as described in the text around Eq. (65). The bias-corrected data are only available up to  $t_0/a = 12$  on these plots, but sloppy only data are plotted in the gray shaded region to demonstrate convergence to a plateau. In the isospin 0 channel, the vacuum state is seen in the unmodified and thermal subtraction-only schemes, so the “first  $\pi\pi$ ” state corresponds to the first excited state energy instead of the ground state.

takes its place as  $aE_2$ . Investigation of this spurious state reveals that the only way to remove this state is to remove the scalar operator from the operator basis, which also shifts of the other effective energies outside of their statistical uncertainty. This spurious state is most likely a fit artifact from a slight over- or under-subtraction of one of the contaminants that has been amplified by the GEVP. No such spurious state appears in the spectrum when the time series subtraction scheme is used, backing up this claim. To avoid this issue, results are taken for sufficiently large times such that no such spurious state is present and both the time series subtraction corrected vacuum subtraction schemes produce consistent results.

The final spectrum results are obtained by increasing  $\delta t = t - t_0$  and  $t_0$  until the GEVP eigenvalues plateau within statistics. This strategy has the advantage of being sufficiently simple without the need to introduce correlator fitting and the corresponding systematics. The data approach these plateau values exponentially, where the exponent is proportional to the energy gap between the largest state that is constrained by the GEVP and the next most significant state that is not sufficiently constrained by the basis of correlators. The operator basis used in this study is composed of the quark bilinear operators and  $\pi\pi$  operators with various back-to-back momenta, so states with similar particle content (namely the finite volume  $\sigma$  state and the  $\pi\pi$  states) are expected to be well-constrained by the basis choice. The remaining poorly-constrained states are then expected to be made up of states that are not well represented by the operator basis, most likely consisting of states that involve two-particle scattering with an excited pion ( $\pi\pi^*$ ). Better overlap with these states could be achieved with an operator basis including derivatives within the quark bilinears that make up the two-particle interpolating oper-

Isospin	matrix element subtraction						time series subtraction					
	24ID			48I			24ID			48I		
	$\delta t$	$t_0$	$N_{\text{op}}$	$\delta t$	$t_0$	$N_{\text{op}}$	$\delta t$	$t_0$	$N_{\text{op}}$	$\delta t$	$t_0$	$N_{\text{op}}$
2	3	7	5	3	11	5	3	6	5	3	8	5
0	3	7	6	3	11	6	3	6	6	3	8	6

TABLE IX. Parameter choices used in the GEVP analysis for this study.  $t$  and  $t_0$  are defined in Eq. (22), with  $\delta t = t - t_0$ .  $N_{\text{op}}$  is the size of the operator basis, where the set of operators used is described in the text.

ators [32, 44].

The GEVP parameters for each isospin channel and ensemble are given in Table IX. These values will have residual contamination from excited states that depends on  $t_0$  and  $\delta t$ , which are estimated in two systematic uncertainties obtained by shifting either  $t_0 \rightarrow t_0 - 1$  or  $\delta t \rightarrow \delta t - 1$  and taking the difference of central values between this result and the nominal choice.

The noninteracting  $\pi\pi$  correlators in this study were used in both the isospin 0 and isospin 2 channels. The isospin 2 channel has no resonance states to spoil the identification of dispersion states. We did not investigate correlating the interacting  $\pi\pi$  spectrum with linear combinations of the energy levels in the noninteracting spectrum. This strategy could be useful for the isospin 0, where a weak resonant state should be present, and might be able to amend this method for future use in the isospin 1 channel where there is a strong overlap with the  $\rho$  resonance state. In the isospin 0 channel, the improvement in statistics from applying this method is negligible and the statistical precision is not sufficient to identify any resonant behavior. However, correlating the interacting correlators with their noninteracting counterparts

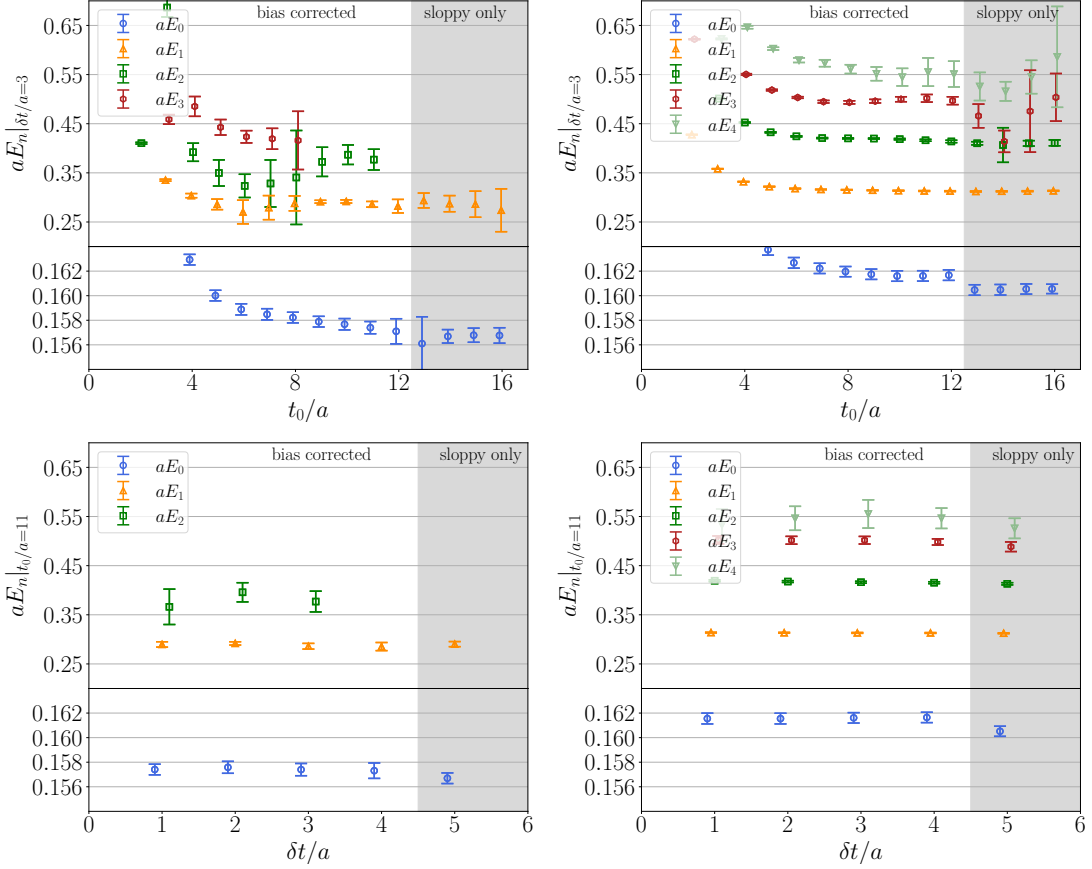


FIG. 5. Plots of the spectrum of states obtained from solving the GEVP on the 48I ensemble. The left (right) plot shows the results for the GEVP applied to the isospin 0 (isospin 2) channel. The top (bottom) panels show the state effective energies as a function of  $t_0/a$  ( $\delta t/a$ ) with fixed  $\delta t/a$  ( $t_0/a$ ). The vertical axis is the effective energy of the states implied by the GEVP. For each plot, multiple state progressions are shown with separate symbols and colors. Each panel has an inset to zoom in on the lowest state's effective energy. The unshaded region has the full AMA procedure applied to correct for bias, while the shaded region is only obtained from low-precision solves and does not correct for this bias. The bias can be significant on the level of the statistical precision, as is seen in the lowest effective energies (blue circles) in the upper-right panel.

is still advantageous because it reduces systematics from lattice cutoff effects.

The spectrum obtained by solving the GEVP for all of the isospin channels as well as the noninteracting values obtained from the process described in Sec. II G are given in Tables X and XI. In addition to the raw values, the correlated energy differences between the interacting and noninteracting spectra are also provided. Tables X and XI give the spectrum results for all isospin channels in the rest frame for the 24ID and 48I ensembles, respectively.

## V. SCATTERING LENGTH AND PHASE SHIFT RESULTS

The  $\pi\pi$  scattering phase shifts are obtained by applying the Lüscher formalism in Eqs. (41)–(44) to the spectra that are obtained from the correlation function data. The deviation of the measured spectra away from their

noninteracting values encodes the strength of the interaction, and the sign indicates whether the interaction is attractive or repulsive. There is no resonance present in the isospin 2 channel, so little deviation from the noninteracting spectrum is expected. In the isospin 0 channel however, the presence of the  $\sigma$  resonance will contribute to shifts away from the noninteracting spectrum, which yields a positive phase shift at energies above threshold.

The uncertainty due to discretization effects up to this point has not been considered because all comparisons have been performed on a single ensemble. When comparing results to the continuum and to other ensembles, it is important to quantify this uncertainty. Although this analysis uses results from two ensembles with different lattice spacings, these ensembles use different lattice actions and so cannot be combined together to come up with a direct estimate of discretization effects. To circumvent this difficulty, we employ the same strategy as our sister paper [5] of using the average of several other

$n$	$aE_n$			$a(E_n - E_n^{\text{NI}})$	
	NI	I=0	I=2	I=0	I=2
0	0.28032(68)(01)	0.2729(18)(03)	0.28273(69)(06)	-0.0075(16)(03)	0.002407(74)(57)
1	0.5917(12)(04)	0.5520(94)(19)	0.6061(15)(03)	-0.0398(91)(23)	0.01440(55)(13)
2	0.7874(25)(14)	0.764(55)(03)	0.8141(42)(04)	-0.024(56)(02)	0.0267(30)(11)
3	0.9434(55)(20)	–	0.961(20)(09)	–	0.018(17)(07)
4	1.063(15)(02)	–	1.055(43)(24)	–	-0.008(43)(26)

TABLE X. A list of the  $\pi\pi$  spectrum in each isospin channel for the 24ID ensemble.  $n$  is an index identifying which state is listed. Columns under the  $aE_n$  heading are the unmodified spectrum results in lattice units, and the columns under  $a(E_n - E_n^{\text{NI}})$  are correlated differences between the interacting and noninteracting  $\pi\pi$  energy levels. As a reference, the column labeled “NI” gives the noninteracting  $\pi\pi$  energy levels obtained from a  $1 \times 1$  GEVP with  $\delta t/a = 3$  and  $t_0/a = 4$ . Note that the energy differences are computed using the same choice of  $\delta t$  and  $t_0$  for both the interacting and noninteracting energy levels, so the differences are not computed with the values in the “NI” column. All quantities include both statistical and systematic errors.

$n$	$aE_n$			$a(E_n - E_n^{\text{NI}})$	
	NI	I=0	I=2	I=0	I=2
0	0.16074(42)(03)	0.15740(50)(33)	0.16161(42)(06)	-0.00334(32)(32)	0.000870(66)(62)
1	0.3075(08)(07)	0.2860(58)(81)	0.3131(09)(07)	-0.0215(59)(74)	0.00562(20)(08)
2	0.4057(16)(07)	0.377(21)(21)	0.4163(19)(27)	-0.029(21)(21)	0.0105(11)(21)
3	0.4854(40)(20)	–	0.5018(77)(19)	–	0.0163(59)(27)
4	0.5568(90)(26)	–	0.555(29)(14)	–	-0.002(29)(16)

TABLE XI. Same as Table X, but for the 48I ensemble. The “NI” column of data is taken at  $\delta t/a = 3$  and  $t_0/a = 10$ .

discretization error coefficients

$$|c_{\text{avg}}^X| = \frac{1}{4} \left( |c_f^X| + |c_{f(\kappa)}^X| + |c_{\sqrt{t_0}, a}^X| + |c_{w_0, a}^X| \right) \quad (66)$$

using the prefactor coefficients listed in Table XVII of Ref. [45]. Here, the superscript  $X$  is used to denote the action ID (I) for the 24ID (48I) ensemble. From this quantity, a fractional discretization uncertainty is assigned for the energy

$$\frac{\delta E_X}{E_X} = |c_{\text{avg}}^X| a_X^2. \quad (67)$$

In the case that the energy difference  $\Delta E_{\pi\pi}$  is used instead, as in Eq. (51), the fractional discretization error is instead applied to  $\Delta E_{\pi\pi}$ . No discretization error is needed on  $M_\pi$  since it is assumed to be free from discretization errors during the scale setting procedure. For the 24ID (48I) ensemble, the fractional uncertainty for discretization effects  $\delta E/E$  comes out to be about 2.5% (1.1%).

The phase shifts computed here assume that only the lowest partial wave allowed by symmetry contributes appreciably and all other higher partial waves are suppressed. All of the data in this study transform under the  $A_1$  octahedral irrep, for which the  $\ell = 4$  partial wave is the next-lowest partial wave with nonvanishing coupling. Coupling of the higher partial wave is expected to be significantly suppressed compared to the lowest  $\ell = 0$  partial wave due to a coupling dependent on the momentum or angular momentum. Under this assumption, no

model of the mixing between partial waves as a function of energy is needed to compute the phase shifts and the values obtained from the lattice may be directly compared with phenomenological estimates.

Although the Lüscher formalism works well for two-particle states, the formalism is expected to break down when thresholds for creation of more than two particles open up. For the scattering channels in this study, the lowest of these thresholds is the four-pion threshold at  $\sqrt{s} = 4M_\pi \approx 0.55$  GeV, which sits just below (above) the first excited state of the 24ID (48I) ensemble in both isospin channels. Although there is no strictly valid interpretation of the scattering phase shifts above this threshold, the data are still plotted so the breakdown of the data from more complicated channels may be qualitatively examined. Three-pion states do not contribute to the correlation functions in this study because they are forbidden by  $G$ -parity symmetry.

### A. Scattering Phase Shifts

Fig. 6 shows the scattering phase shifts in the isospin 2 channel as a function of the center of mass energies of the  $\pi\pi$  system for both the 24ID and 48I ensembles. The data plotted here correspond to the “thermal subtraction” method of Eq. (26). Two phenomenological curves are also plotted; the first was computed using next-to-next to leading order SU(2) chiral perturbation theory [46, 47]. The second uses integral equations for

the scattering phase shifts first derived by Roy [48–50]. Specifically, we use the results of Ref. [49] to calculate an error band for a qualitative comparison against our results. A comprehensive study involving the more accurate prediction in Ref. [50] is deferred to a future publication. The top row of the figure shows the interacting  $\pi\pi$  data using Eq. (49) to compute the center of mass momentum. Considering only statistical uncertainties, the two ensembles have good agreement for the ground state and first excited state, and agreement up to systematic uncertainties for the second excited state at larger  $\sqrt{s}$ . The systematic uncertainty due to discretization effects completely dominates the total uncertainty, leading to a result that is mostly consistent with zero.

In the middle row of Fig. 6, Eq. (51) is used together with the noninteracting  $\pi\pi$  energies to compute the phase shift instead, which leads to a reduction in statistical error. The dominant systematic uncertainty due to discretization effects is reduced dramatically, resulting in roughly comparable statistical and systematic uncertainties. The excited states in the  $\pi\pi$  correlation functions are also correlated between the interacting and noninteracting energies and their effects are reduced when taking the difference. This accounts for the large shift in the second excited state energy, leading to better agreement between the two ensembles.

However, the subtraction between interacting and noninteracting energies also produces a large discrepancy between results for the ground state. This discrepancy is due to the introduction of backward-propagating terms in the noninteracting correlation functions of Eq. (46),

$$\begin{aligned} C_{\pi\pi,\mathbf{P},-\mathbf{P}}^{\text{NI}}(t) &= C_{\pi,\mathbf{P}}(t)C_{\pi,-\mathbf{P}}(t) \\ &= \sum_{mn} |\langle 0|\mathcal{O}_{\pi,\mathbf{P}}|\pi^0\rangle_m|^2 |\langle 0|\mathcal{O}_{\pi,\mathbf{P}}|\pi^0\rangle_n|^2 \\ &\quad \times \left( e^{-E_{\pi,m}t - E_{\pi,n}t} + e^{-E_{\pi,m}t - E_{\pi,n}(T-t)} \right. \\ &\quad \left. + e^{-E_{\pi,m}(T-t) - E_{\pi,n}t} + e^{-E_{\pi,m}(T-t) - E_{\pi,n}(T-t)} \right). \end{aligned} \quad (68)$$

The terms suppressed by  $e^{-ET}$  produce small but non negligible shifts in the noninteracting correlation function and a large shift in the correlated difference between interacting and noninteracting energies. The solution is to replace the noninteracting correlation function with a thermally-subtracted correlator that removes the contributions including backward-propagating pions,

$$\begin{aligned} C_{\pi\pi,\mathbf{P},-\mathbf{P}}^{\text{NI,sub}}(t) &= C_{\pi\pi,\mathbf{P},-\mathbf{P}}^{\text{NI}}(t) \\ &\quad - |\langle 0|\mathcal{O}_{\pi,\mathbf{P}}|\pi^0\rangle|^2 |\langle 0|\mathcal{O}_{\pi,\mathbf{P}}|\pi^0\rangle|^2 \left( 2e^{-E_\pi T} + e^{-2E_\pi(T-t)} \right), \end{aligned} \quad (69)$$

where only the 0-momentum backward-propagating term is relevant. The subtracted correlator from Eq. (69) is used in place of the unsubtracted noninteracting correlator of Eq. (46) to produce the bottom row of Fig. 6. In

this pair of plots, removal of the backward-propagating pion terms restores the agreement between the ground-state energies in the phase shift and has negligible impact on the higher excited states. This subtraction also removes much of the systematic error, which is attributed to a mismatch in the energies of the interacting and noninteracting values.

The combination of thermal subtractions on the interacting and noninteracting correlation functions as well as the correlated subtraction between interacting and noninteracting energies produces a set of phase shifts for each ensemble that are consistent with each other and agree well with the result from the Roy Equation. This remains true even after passing the threshold for production of four-pion states, where there is no expectation that the Lüscher phase shift quantization condition still holds. There is also good agreement with the  $\text{SU}(2)\chi\text{PT}$  expectation for the lowest energy state, as depicted in the lower-right panel of Fig. 6. The validity of  $\chi\text{PT}$  is however expected to break down at large  $\sqrt{s}$ , which spoils the comparison with higher excited states.

Fig. 7 shows the scattering phase shifts in the isospin 0 channel as a function of the center of mass energies of the  $\pi\pi$  system for both the 24ID and 48I ensembles. All data here correspond to the “thermal+corrected vacuum” subtraction in Eqs. (36)–(38). The top plot shows the scattering phase shift computed from only the interacting correlator data, which have large statistical uncertainties. In the bottom plot, the difference between interacting and noninteracting energies are again applied, but the statistical fluctuations of the two spectra are not correlated enough to produce a noticeable reduction in statistical error. The systematic error due to discretization uncertainty is reduced after the subtraction, resulting in a phase shift that is largely dominated by the statistical uncertainty and demonstrating that the lattice spacing uncertainty in the isospin 0 channel is not appreciable. For the 48I ensemble, there is an approximate factor of 2 reduction in the statistical uncertainty on the ground state energy due to the subtraction, which is not visible in Fig. 7 because the energy is below threshold and therefore corresponds to imaginary  $q$ .

## B. Scattering Lengths

The computed spectra on each ensemble close to threshold may also be used to produce estimates of the parameters associated with the effective range expansion. The effective range expansion is expressed as the relation

$$p \cot \delta_{I\ell}(pL/2\pi) = \frac{1}{a_{I\ell}} + \frac{1}{2} r_{I\ell} p^2 + O(p^4), \quad (70)$$

where  $I$  and  $\ell$  correspond to the isospin and spin channels, and  $a_0$  and  $r_0$  are the scattering length and effective range, respectively. Taking  $q = pL/2\pi$  close to threshold, the terms proportional to higher powers of  $p^2$  can be neglected and the scattering length computed directly from

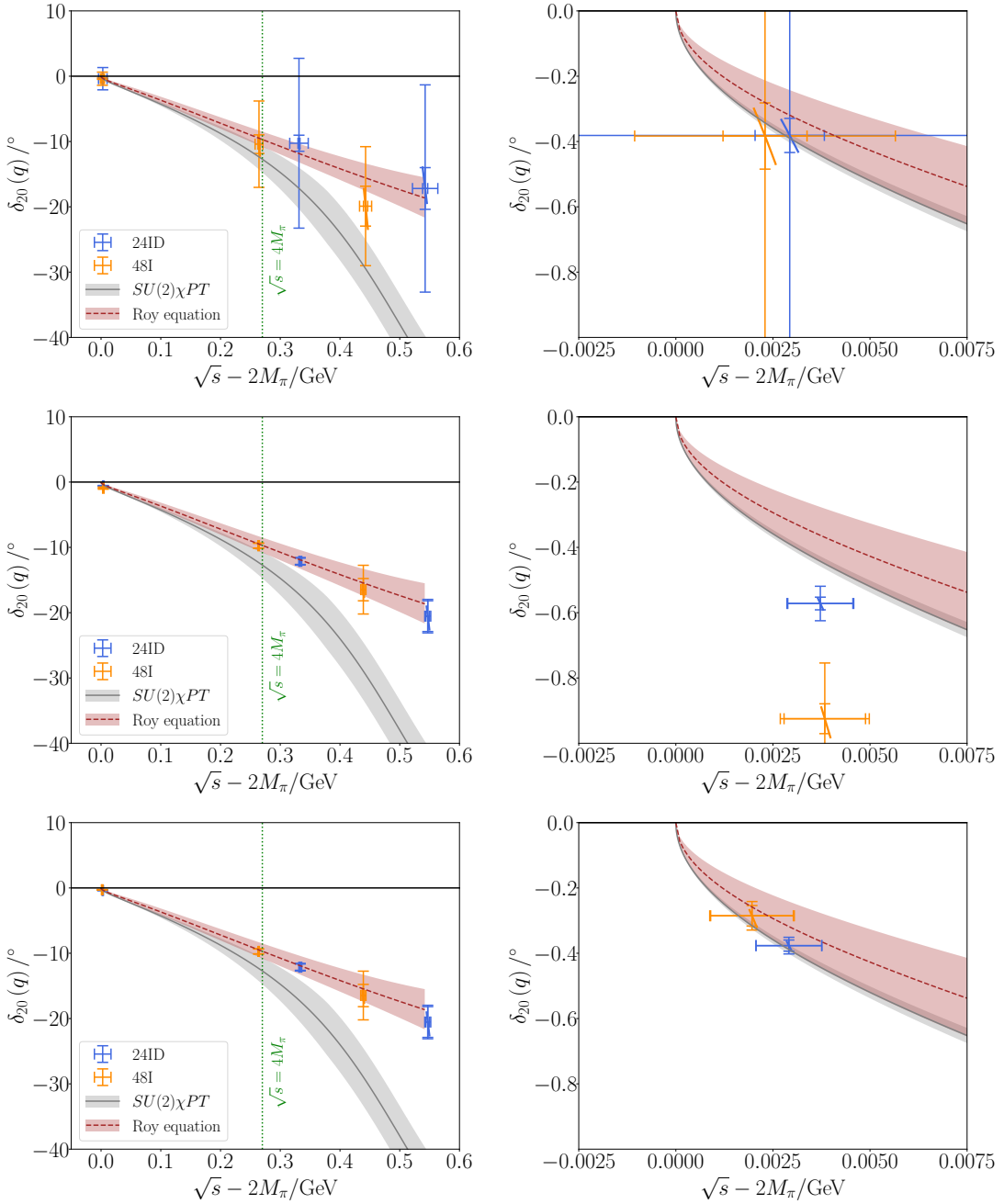


FIG. 6. Phase shift plots for the lattice data in the isospin 2 channel. The left column shows the phase shifts as a function of center of mass energy  $\sqrt{s}$ , and the right column is the same plot zoomed in to near the threshold value. The center of mass energy has been shifted by  $2M_\pi$  to account for slight differences in the pion mass. The blue (orange) denote the 24ID (48I) ensemble results. In addition to the statistical and systematic error bars, a curve has been plotted on top of each scatter point that follows the Lüscher quantization curve over the range of phase shifts covered by the middle 68% of the jackknife samples at fixed pion mass. Phenomenological curves using Roy Equation and  $SU(2)$  chiral perturbation theory have been plotted for comparison. The Roy equation uncertainty band from Ref. [49] is plotted to demonstrate the good agreement with the LQCD scattering data at low center of mass energies. A vertical dotted green line is included to show the  $4\pi$  threshold cutoff, above which the Lüscher quantization condition is expected to break down. The top row shows the results obtained using only the interacting energies obtained from the lattice simulation, reported under the  $I=2$  column in the left half of Tables X and XI. The middle row shows the results using the spectrum obtained from the procedure using the difference between interacting and noninteracting energies described in Sec. II G. The bottom row shows again the results using the spectrum with the difference between interacting and noninteracting energies, but additionally subtracts away the backward-propagating contributions in the noninteracting correlation functions, as described in Eq. (69).

the ground state energy,

$$q \cot \delta_{I\ell}(q) \Big|_{q \ll 1} = \frac{L}{2\pi a_{I\ell}} + O(q^2). \quad (71)$$

From the Lüscher relation, the phase shift in the spin-0 channel with generic isospin  $I$  is written

$$\frac{\mathcal{Z}_{00}(1; q^2)}{\pi^{\frac{3}{2}}} = q \cot \delta_{I0}(q), \quad (72)$$

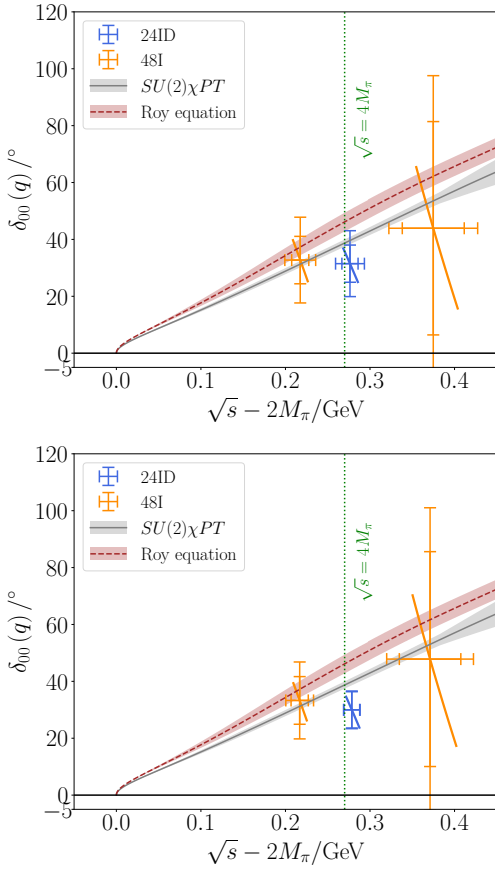


FIG. 7. Phase shift plots for the lattice data in the isospin 0 channel. The description for the top (bottom) plot is the same here as for the top (bottom) plot in the left column of Fig. 6. The energies plotted here correspond to  $n = 1$  and  $2$  in the  $I = 0$  columns of Tables X and XI. Note that the  $n = 0$  point close to threshold is not shown because  $q^2 < 0$  cannot be mapped to a real value of  $\sqrt{s}$ . The Roy equation uncertainty band is calculated from Ref [49].

which when combined with Eq. (71) may be used to estimate the scattering length.

The pion mass times scattering lengths obtained by applying the both the time series subtraction (Eq. (31)) and matrix element subtraction (the “corrected vacuum+thermal subtraction” for isospin 0 and “thermal subtraction” for isospin 2) schemes combined with the difference between interacting and noninteracting effective energies (Eq. (48)) are given in Tables XII and XIII for the isospin 0 and isospin 2 channels, respectively. These tables give the full breakdown of statistical and systematic uncertainties on the computed scattering lengths. For the matrix element subtraction scheme on the 48I ensemble, the scattering lengths obtained for both the isospin 0 and 2 channels are in excellent agreement with phenomenology [51]. These values will be taken as our final results when comparing to other literature.

We find reasonable agreement between the determinations of the scattering lengths on both ensembles us-

Ens	$M_\pi a_{00}$ (matrix element subtraction)
24ID	$0.184(46)_{\text{stat}}(00)_{1\pi}(08)_{t_0}(04)_{\delta t}(05)_{a^2}(01)_{3\text{pt}}[47]_{\text{total}}$
48I	$0.218(24)_{\text{stat}}(00)_{1\pi}(19)_{t_0}(15)_{\delta t}(03)_{a^2}(00)_{3\text{pt}}[34]_{\text{total}}$
Ens	$M_\pi a_{00}$ (time series subtraction)
24ID	$0.214(28)_{\text{stat}}(00)_{1\pi}(17)_{t_0}(12)_{\delta t}(06)_{a^2}[35]_{\text{total}}$
48I	$0.125(41)_{\text{stat}}(00)_{1\pi}(53)_{t_0}(41)_{\delta t}(02)_{a^2}[79]_{\text{total}}$

TABLE XII. Results for the pion mass times the scattering length in the isospin 0 channel,  $M_\pi a_{00}$ , for each ensemble and subtraction scheme. The values in this table are computed assuming Eqs. (71) and (72) and using only the ground state energy. The full breakdown of uncertainties is included; stat denotes the statistical uncertainty,  $1\pi$  denotes the uncertainty due to excited states in the  $1\pi$  fits as described in Sec. IV A 1,  $t_0$  and  $\delta t$  denote the uncertainty from shifting the corresponding time variable in Eq. (64) by 1 timeslice, 3pt denotes the uncertainty on the ratio with a pion transition matrix element in Eq. (58) as described in Sec. IV A 2,  $a^2$  denotes the discretization uncertainty applied as described in Eq. (67), and the number in square brackets is the total uncertainty on the quantity after adding all errors in quadrature. For the time series subtraction scheme, the pion transition matrix elements are unused and so their systematic uncertainty is not included in the error budget. Uncertainties are computed using standard error propagation and the uncertainties from similar sources are added in quadrature.

Ens	$M_\pi a_{20}$ (matrix element subtraction)
24ID	$-0.0500(15)_{\text{stat}}(00)_{1\pi}(11)_{t_0}(03)_{\delta t}(12)_{a^2}(01)_{3\text{pt}}[22]_{\text{total}}$
48I	$-0.0477(35)_{\text{stat}}(00)_{1\pi}(20)_{t_0}(26)_{\delta t}(05)_{a^2}(01)_{3\text{pt}}[48]_{\text{total}}$
Ens	$M_\pi a_{20}$ (time series subtraction)
24ID	$-0.0519(27)_{\text{stat}}(00)_{1\pi}(25)_{t_0}(14)_{\delta t}(12)_{a^2}[41]_{\text{total}}$
48I	$-0.0450(53)_{\text{stat}}(00)_{1\pi}(28)_{t_0}(39)_{\delta t}(05)_{a^2}[71]_{\text{total}}$

TABLE XIII. The same as Table XII, but for the isospin 2 channel.

ing both subtraction schemes within their uncertainties, and with phenomenological determinations from Caprini *et al.* [51]. The largest disagreements appear for the 24ID ensemble in the isospin 2 channel. This is likely due to 1) the uncontrolled large discretization errors from the large lattice spacing, and 2) a statistical fluctuation to a low pion mass combined with an underestimated uncertainty from too few statistical measurements. The low pion mass would cause the noninteracting effective energy to be underestimated and increase the interacting-noninteracting effective energy difference, which produces a larger negative scattering length in competition with the explicit pion mass dependence in the product  $M_\pi a_{20}$ . This should also produce a smaller  $a_{00}$  in the isospin 0 channel on the 24ID ensemble, although the uncertainties are large enough that the disagreement is not as obvious.

Another possible cause for concern is the isospin 0 scattering length for the matrix subtraction scheme on the 48I ensemble. This estimate is quite low in comparison

to the phenomenological value when only the statistical uncertainty is considered. This is due to a large excited state contamination in the *noninteracting*  $\pi\pi$  correlators that is amplified by the time series subtraction scheme. The contamination is strongly correlated with the isospin 2 channel interacting correlators but absent from the isospin 0 channel. When the interacting-noninteracting effective energy difference is taken, the excited state contamination largely cancels in the isospin 2 channel but is introduced to the isospin 0 channel by the subtraction. This large contamination is reflected in the large  $t_0$  and  $\delta t$  systematic uncertainties on  $M_\pi a_{00}$  and the correspondingly large total uncertainty.

The effective range expansion of Eq. (70) is shown in Fig. 8. In both isospin channels, the data close to threshold are in good agreement with the predictions from SU(2) chiral perturbation theory and the Roy equation. One might hope to obtain information about the effective range  $r_{I\ell}$  in Eq. (70) by taking into account both the ground state and first excited state. This would amount to fitting the  $p^2$  dependence in Fig. 8 with the right-hand side of Eq. (70), specifically to access the information about the slope with respect to  $p^2$  at threshold:

$$2 \frac{\partial}{\partial p^2} [p \cot \delta_{I\ell}(q)] = r_{I\ell}. \quad (73)$$

The nontrivial  $p^2$  dependence of the SU(2) chiral perturbation theory and Roy equation predictions over the range of  $p^2$  between the ground state and first excited state suggest that the  $p^2$  dependence must include higher-order corrections that are not properly captured by the formula in Eq. (70). With the data available, the best that can be done is to fit the linear response with respect to  $p^2$ , which will not reproduce the correct slope. For this reason, no attempt is made to determine the effective range from the lattice data and the first excited state is plotted in Fig. 8 only to show consistency with the phenomenological predictions. It should be noted, however, that a linear extrapolation between the ground state and first excited state gives a scattering length that is consistent with the estimate from the ground state alone to well within  $1\sigma$ , indicating that the error from computing the scattering length at nonzero  $q^2$  is negligible.

## VI. DISCUSSION & CONCLUSIONS

In this analysis, we solved the GEVP for matrices of correlation functions computed with large bases of one- and two-bilinear interpolating operators in LQCD, obtaining scattering lengths for both the isospin 0 and isospin 2 channels. These results take advantage of the distillation framework to compute and subtract away contamination from unwanted thermal and vacuum contributions to the two-pion correlation functions. By correlating the computed spectrum with another obtained from products of single pion correlation functions, we

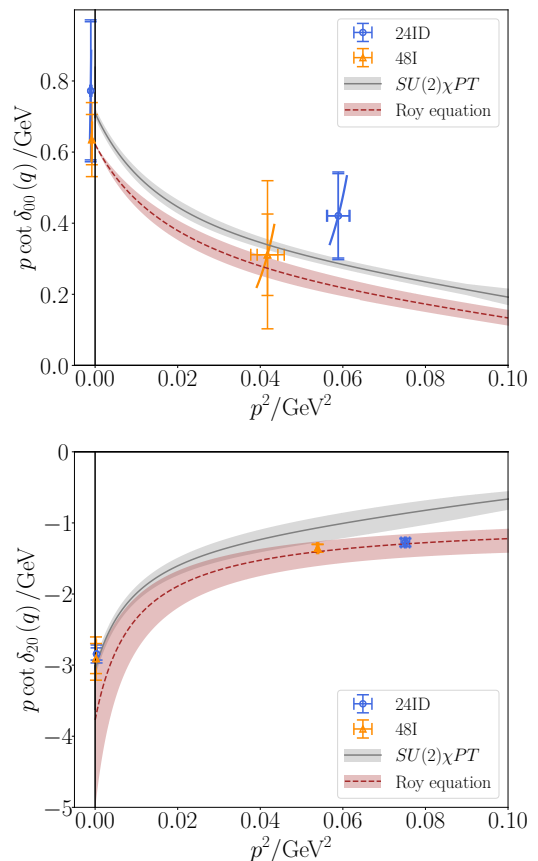


FIG. 8. Plot of the effective range expansion of Eq. (70) as a function of  $p^2$ . Data for the ground state and first excited state of both ensembles are plotted as well as the predictions from SU(2) chiral perturbation theory and the Roy equation. Like Fig. 6, a curve has been plotted on top of each data point that follows the Lüscher quantization curve at fixed pion mass over the range of phase shifts covered by the middle 68% of the jackknife samples.

were able to improve the precision on the isospin-2 channel scattering lengths.

Our analysis constitutes the first effort to obtain the isospin 0 scattering length from LQCD with both valence and sea quarks at physical pion mass and the second to achieve this claim in the isospin 2 channel. Although our results use two ensembles of different lattice spacings, these ensembles have different quark actions and so lie on different continuum trajectories. To attempt to account for the possible discretization errors, a fractional uncertainty is assigned to the  $\pi\pi$  state energy based on  $a^2$  scaling behavior of other parameters on the same lattice actions. Despite the unknown discretization effects, the 48I ensemble produces scattering lengths for both the isospin 0 and isospin 2 channels that are consistent with phenomenology within their quoted statistical uncertainties. This is the third work in a series of RBC+UKQCD collaboration sister papers to understand  $\pi\pi$  scattering [5, 52]. Comparisons between the results

presented here and its sister works is deferred to a future paper, which will combine the results of these works with phenomenology.

A comparison of these results to literature values for the scattering lengths from the FLAG review [53] are given for both isospin channels in Table XIV. The values from the tables are also given in a summary plot in Fig. 9. One other LQCD computation has been performed directly at physical  $M_\pi$ , labeled as “ETM 20,” which obtained the scattering phase shift in the isospin 2 channel [23]. This result is in good agreement with our isospin 2 result and with a comparable uncertainty to our extraction. All of the other results are computed at heavier-than-physical pion masses and extrapolated down to the physical point, which all tend to have reasonable agreement with phenomenological estimates. The majority of these have a lightest pion mass at the level of  $M_\pi \approx 250$  MeV and several ensembles for extrapolations to lighter pion masses.

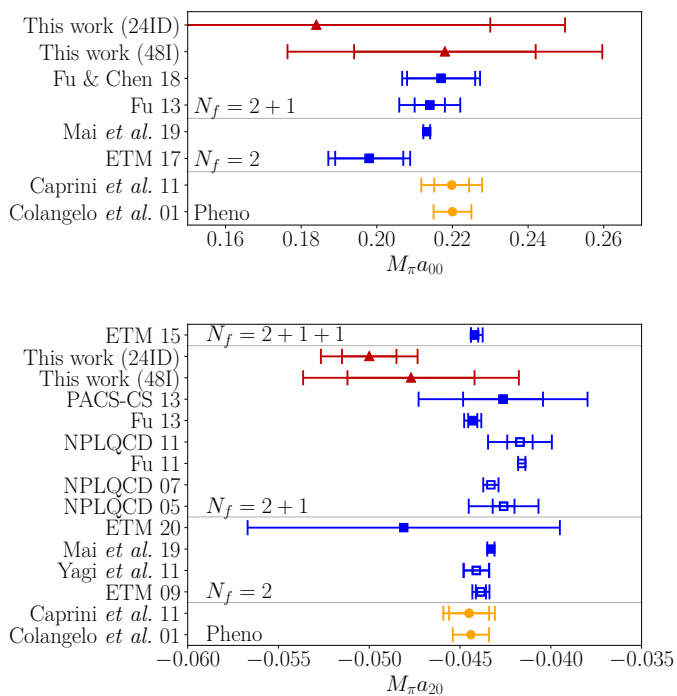


FIG. 9. Summary plot of other  $\pi\pi$  scattering length calculations from LQCD and phenomenology. Results plotted here are taken from the FLAG review [53], with the addition of ETM 20 [23] and Mai *et al.* 19. Results with a smallest  $M_\pi \leq 250$  MeV are plotted with filled symbols, all others with open symbols. The full list of references is found in Table XIV.

The distillation setup that was used in this analysis is of great interest to the RBC+UKQCD collaborations’ effort to compute the anomalous magnetic moment of the muon [66]. For this purpose, distillation perambulators have been generated on several other ensembles, including 2 other ensembles at physical pion mass (correspondingly referred to as 64I and 96I) at finer lattice spacing

using the same action as the 48I. An identical analysis could be carried out on these ensembles to facilitate a proper continuum extrapolation entirely at the physical pion mass in order to assess discretization effects on the scattering lengths and phase shifts. Correlation of these distillation data with the point vector current insertions needed for the  $g - 2$  analysis would provide additional constraints on the isospin 1 channel, which was ignored for the purposes of this analysis.

Distillation is also ideal for constructing additional correlation functions without the need for additional solutions of the Dirac matrix. These advantages permit studies of moving frames [67], different operator smearings [32, 44], and other cubic group irreducible representations [68] with little extra cost. This would allow the phase shift to be probed at more center of mass energies below the  $4\pi$  production threshold, allowing the phase shift curve and the effective range expansion to be mapped out in more detail. This could also be used to constrain the strength of the D-wave  $\pi\pi$  scattering channel.

For the moving frames, the subtraction techniques using other correlation functions that are described in this manuscript are especially powerful. At nontrivial center-of-mass momentum, the appropriate transition matrix elements for assessing the thermal contamination to the  $\pi\pi$  two-point correlation functions connect in states and out states with different momenta. This produces a nontrivial Euclidean time dependence that does not exactly cancel with the time series subtraction method in Eq. (31). Other subtraction schemes have been adopted to circumvent this flaw [67], but these subtractions are only approximate and still suffer from the enhancement of excited state contamination that appeared in the 48I ensemble in this analysis. It is also possible to fit this correlator contamination directly, but the exponential suppression with the temporal extent makes this prospect challenging. Construction of alternative correlation functions provides a complimentary method for constraining the required matrix elements without enhancing excited state contamination or competing with the exponential suppression.

The phase shifts computed in this analysis are in excellent agreement with the scattering phase shift parameterization from Roy [48]. This is true even beyond the  $4\pi$  threshold, where the Lüscher quantization condition is not strictly valid. This bodes well for future analyses, suggesting that the corrections to the spectrum from mixing with  $4\pi$  states are small and that it might be possible to understand these contaminations as only a perturbation on elastic scattering phase shift results.

With correlation functions computed directly with physical pion mass, at several lattice spacings and volumes, and moving frames, LQCD will soon be able to make definitive claims about scattering in the  $\pi\pi$  channels at various isospin. These results could become competitive with phenomenological estimates in the near future, especially for higher partial wave contributions, and

Authors	$N_f$	Ref.	$M_\pi a_{00}$	$M_\pi \geq [\text{MeV}]$	$N_{\text{ens}}$
This work (48I)	2+1	—	0.218(24)(24)	139	1
Mai <i>et al.</i> 19	2	[54]	0.2132(9)	220	6
Fu & Chen 18	2+1	[55]	0.217(9)(5)	247	3
ETM 17	2	[56]	0.198(9)(6)	250	3
Fu 13	2+1	[57]	0.214(4)(7)	240	6
Caprini <i>et al.</i> 11	—	[51]	0.2198(46)(16)(64)	—	—
Colangelo <i>et al.</i> 01	—	[50]	0.220(5)	—	—

Authors	$N_f$	Ref.	$M_\pi a_{20}$	$M_\pi \geq [\text{MeV}]$	$N_{\text{ens}}$
This work (48I)	2+1	—	-0.0477(35)(33)	139	1
ETM 20	2	[23]	-0.0481(86)	134	3
Mai <i>et al.</i> 19	2	[54]	-0.0433(2)	220	6
ETM 15	2+1+1	[58]	-0.0442(2) <sub>(6)</sub> <sup>(4)</sup>	250	11
PACS-CS 13	2+1	[59]	-0.04263(22)(41)	170	1*
Fu 13	2+1	[57]	-0.04430(25)(40)	240	6
NPLQCD 11	2+1	[60]	-0.0417(07)(02)(16)	390	4
Fu 11	2+1	[61]	-0.0416(2)	330	1*
Yagi <i>et al.</i> 11	2	[62]	-0.04410(69)(18)	290	1*
ETM 09	2	[63]	-0.04385(28)(38)	270	6
NPLQCD 07	2+1	[64]	-0.04330(42)	290	4
NPLQCD 05	2+1	[65]	-0.0426(06)(03)(18)	290	3
Caprini <i>et al.</i> 11	—	[51]	-0.0445(11)(4)(8)	—	—
Colangelo <i>et al.</i> 01	—	[50]	-0.0444(10)	—	—

TABLE XIV. Most recent results for the isospin 0 and isospin 2 scattering lengths, compiled in the FLAG review [53]. Additional references for “ETM 20” and “Mai *et al.* 19” are listed which has appeared in the literature after the FLAG review. Minimum valence pion mass for each reference, in GeV, is listed in the fifth column and the number of ensembles that were used in each reference in the sixth column. For the three references where only one ensemble was used, multiple valence pion masses were computed. “PACS-CS 13” had a total of 5 valence pion masses, while both “Fu 11” and “Yagi *et al.* 11” had 6 valence pion masses.

provide an alternative theoretical prediction of the low energy constants relevant to pion scattering.

## VII. ACKNOWLEDGEMENTS

We would like to thank our colleagues in the RBC and UKQCD collaborations for their interesting discussions. The research of M.B. is funded through the MUR program for young researchers “Rita Levi Montalcini”. The work of D.H. is supported by the Swiss National Science Foundation (SNSF) through grant No. 200020.208222. T.I. and C.L. were supported in part by US DOE Contract DESC0012704(BNL), and T.I. was supported in part by the Scientific Discovery through Advanced Computing (SciDAC) program LAB 22-2580. The work of A.S.M. was supported by the Department of Energy, Office of Nuclear Physics, under Contract No. DE-SC00046548. The work of A.S.M. is also supported in part by Lawrence Livermore National Security, LLC under Contract No. DE-AC52-07NA27344 with the U.S. Department of Energy. The work of M.T. was sup-

ported in part by US DOE awards DE-SC0010339 and DE-SC002114. This work was supported by resources provided by the Scientific Data and Computing Center (SDCC) at Brookhaven National Laboratory (BNL), a DOE Office of Science User Facility supported by the Office of Science of the US Department of Energy. The SDCC is a major component of the Computational Science Initiative at BNL. We gratefully acknowledge computing resources provided through USQCD clusters at BNL and Jefferson Lab.

## Appendix A: Scattering Phase Shift Formalism

Due to the finite volume of calculations in LQCD, it is not possible to isolate an asymptotic state. Particles in multiparticle states will travel through the periodic boundaries and reinteract with each other. These interactions induce deviations in the energy spectrum as the states mix and undergo avoided level crossings. As a result, the spectrum of the multiparticle states observed on the lattice cannot be directly deduced from the infinite

volume continuum spectrum.

However, this problem may be turned on its head by using the finite volume as a probe of the physics of multi-particle scattering. The deviations of the spectrum away from the noninteracting limit are related to the infinite volume scattering phase shifts. It is possible to vary the volume and use the deviations in the spectrum to deduce the scattering phase shifts. This was first proposed by Lüscher in a series of papers [11–13], and was later generalized to moving frames in Ref. [14]. The simplest system that exhibits this behavior with the volume is the  $\pi\pi$  interaction channel, which is target of this study. For the purposes of this appendix, we will discuss  $\pi\pi$  scattering at general center-of-mass momentum, although the entire analysis in this manuscript was performed in the  $\pi\pi$  center-of-mass rest frame only.

The matrix elements may be deduced by computing the shifts in the  $\pi\pi$  energy levels away from the expected infinite-volume continuum values,

$$\mathbf{p}^2 = \frac{1}{4} (E_{\pi\pi}^2 - (2M_\pi)^2 - \mathbf{P}^2), \quad (\text{A1})$$

where the momentum of the moving frame is given by  $\mathbf{P} = 2\pi\mathbf{d}/L$  for  $\mathbf{d} \in \mathbb{Z}^3$ . For convenience, we define the normalized momentum

$$\mathbf{q} = \mathbf{p}L/2\pi. \quad (\text{A2})$$

The scattering phase shifts may then be computed by solving

$$\det [e^{2i\delta(q)} - U(q)] = 0 \quad (\text{A3})$$

for a matrix  $U$  computed from studying the mixing of states in the finite volume,

$$U = (\mathcal{M} + i\mathbb{1})(\mathcal{M} - i\mathbb{1})^{-1} \quad (\text{A4})$$

with the scattering matrix  $\mathcal{M}$  to be given below. The expression for  $\mathcal{M}$  is deduced from  $M$ , the continuous, finite-volume expression coupling the angular momentum eigenstates given by

$$M_{\ell m, \ell' m'}^{\mathbf{d}}(q) = -i\gamma^{-1} \frac{(-1)^\ell}{\pi^{3/2}} \sum_{j=|\ell-\ell'|}^{\ell+\ell'} \sum_{s=-j}^j \left(\frac{2\pi i}{pL}\right)^{j+1} \mathcal{Z}_{js}^{\mathbf{d}}(1; q) C_{\ell m, js, \ell' m'}. \quad (\text{A5})$$

The term  $C$  is proportional to the typical SU(2) Clebsch-Gordan coefficients,

$$C_{\ell m, js, \ell' m'} = \left[ i^{\ell-j+\ell'} \sqrt{\frac{(2\ell+1)(2j+1)}{(2\ell'+1)}} \langle \ell, 0; j, 0 | \ell', 0 \rangle \right] \langle \ell, m; j, s | \ell', m' \rangle, \quad (\text{A6})$$

where the term in square brackets is independent of the angular momentum  $\mathbf{z}$  components,  $m$ ,  $s$ , and  $m'$ . The Lorentz factor  $\gamma$  is computed from the moving frame momentum,

$$\gamma = \frac{1}{\sqrt{1 - \frac{\mathbf{P}^2}{E_{\pi\pi}^2}}}, \quad (\text{A7})$$

and  $\mathcal{Z}^{\mathbf{d}}$  is a spherical derivative of the zeta function,

$$\mathcal{Z}_{\ell m}^{\mathbf{d}}(s; q) = \sum_{\mathbf{r} \in P_{\mathbf{d}}} \mathcal{Y}_{\ell m}(\mathbf{r}) (\mathbf{r}^2 - q^2)^{-s}, \quad (\text{A8})$$

with  $\mathcal{Y}$  proportional to a spherical harmonic,

$$\mathcal{Y}_{\ell m}(\mathbf{r}) = r^\ell Y_{\ell m}(\hat{r}). \quad (\text{A9})$$

The domain of the sum in the expression for  $\mathcal{Z}$  is

$$P_{\mathbf{d}} = \left\{ \mathbf{r} \in \mathbb{R}^3 \mid \mathbf{r} = \hat{\gamma}^{-1} \left( \mathbf{n} + \frac{\mathbf{d}}{2} \right), \mathbf{n} \in \mathbb{Z}^3 \right\}, \quad (\text{A10})$$

with the operator  $\hat{\gamma}^{-1}$  generating a boost of the momentum along the direction of  $\mathbf{d}$ ,

$$\hat{\gamma}^{-1} \mathbf{k} = \gamma^{-1} \mathbf{k}_{\parallel} + \mathbf{k}_{\perp} \quad (\text{A11})$$

for

$$\mathbf{k}_{\parallel} = \frac{\mathbf{k} \cdot \mathbf{d}}{d^2} \mathbf{d}, \quad \mathbf{k}_{\perp} = \mathbf{k} - \mathbf{k}_{\parallel}. \quad (\text{A12})$$

The expression in Eq. (A5) is derived for a theory that is continuous but restricted to finite volume, but the matrix element in Eq. (A6) is expressed in terms of the infinite volume angular momentum eigenstates. These continuum angular momentum eigenstates are considered in the center of mass frame of the  $\pi\pi$  system, which is boosted relative to the lab frame when  $\mathbf{P} \neq \mathbf{0}$ . Another Clebsch-Gordan coefficient must be included to project the system to the irreducible representations of the moving  $\pi\pi$  system.

The center of mass states belong to a reducible representation and are conventionally referred to as canonical states, given simply by a boost of a rest-frame angular momentum eigenstate,

$$\hat{L}(\mathbf{P}) |\mathbf{0}, \ell, m\rangle_{\mathcal{C}} = |\mathbf{P}, \ell, m\rangle_{\mathcal{C}}. \quad (\text{A13})$$

The canonical states are denoted with a subscript  $\mathcal{C}$  and

satisfy the action under rotation given by

$$\hat{R} |\mathbf{P}, \ell, m\rangle_{\mathcal{C}} = \sum_{m'} \mathcal{D}_{m'm}^{\ell}(\hat{R}) |\hat{R}\mathbf{P}, \ell, m'\rangle_{\mathcal{C}}. \quad (\text{A14})$$

The irreducible representations of boosted systems are helicity irreps, with states that satisfy the action under rotation

$$\hat{R} |\mathbf{P}, \ell, \lambda\rangle = |\hat{R}\mathbf{P}, \ell, \lambda\rangle \quad (\text{A15})$$

with  $\lambda = \pm|\lambda|$  denoting the helicity. Combining Eqs. (A13)–(A15) results in the desired relation between canonical and helicity states,

$$\langle \mathbf{P}, \ell, \lambda | \mathbf{P}, \ell, m \rangle_{\mathcal{C}} = \mathcal{D}_{m\lambda}^{\ell*}(\hat{R}_0), \quad (\text{A16})$$

for  $\mathbf{P} = \hat{R}_0 P \hat{z}$  and noting that  $\mathcal{D}_{m\lambda}^{\ell*}(\hat{R}_0) = \mathcal{D}_{\lambda m}^{\ell}(\hat{R}_0^{-1})$ .

There is an additional Clebsch-Gordan coefficient that is needed because the finite volume breaks the continuous rotational symmetry down into the finite octahedral

rotation group. The restriction to the octahedral group is imposed by contracting Eq. (A5) with subduction coefficients, which for properly normalized states may be written as

$$S_{\Lambda^{(n)}, \mu}^{\mathbf{P}, \ell, \lambda} = \langle \Lambda^{(n)}, \mu | \mathbf{P}, \ell, \lambda \rangle. \quad (\text{A17})$$

The index  $\lambda$  denotes helicity when  $\mathbf{P} \neq \mathbf{0}$  or otherwise the  $\mathbf{z}$  component of angular momentum, and  $\mathcal{P}$  denotes the parity of the state. The octahedral group representations  $\Lambda$  have their own set of indices  $\mu$ , which implicitly encode the momentum in the case of moving frames. In some cases, the dimension of the angular momentum irrep may be large enough to permit several embeddings of the same irrep, for which the embedding is distinguished by the additional index  $n$ . These embeddings are unique only up to a unitary change of basis. From sets of known subduction coefficients, other representations can be built up by imposing a tensor product relation,

$$S_{\Lambda^{(n)}, \mu}^{\mathbf{P}, \ell, \lambda} = N \sum_{\mu_1, \mu_2} \sum_{m_1, m_2} \langle \Lambda, \mu | \Lambda_1, \mu_1; \Lambda_2, \mu_2 \rangle S_{\Lambda_1^{(n_1)}, \mu_1}^{\mathbf{P}_1, \ell_1, \lambda_1} S_{\Lambda_2^{(n_2)}, \mu_2}^{\mathbf{P}_2, \ell_2, \lambda_2} \langle \mathbf{P}_1, \ell_1, \lambda_1; \mathbf{P}_2, \ell_2, \lambda_2 | \mathbf{P}, \ell, \lambda \rangle. \quad (\text{A18})$$

This equation may be used to derive the higher-spin subduction coefficients from those of lower-spin.

With the expressions in Eqns. (A16) and (A17), it is now possible to write the full matrix element needed for Eq. (A4),

$$\begin{aligned} \mathcal{M}_{\ell, n; \ell', n'}^{\mathbf{P}, \Lambda}(q) &= \frac{1}{\dim \Lambda_{\mathbf{P}}} \sum_{\mu} \sum_{\lambda, \lambda'} \sum_{m m'} \\ &\times S_{\Lambda^{(n)}, \mu}^{\mathbf{P}, \ell, \lambda} S_{\Lambda^{(n')}, \mu}^{\mathbf{P}, \ell', \lambda'} \mathcal{D}_{m\lambda}^{\ell*}(\hat{R}_0) \mathcal{D}_{m'\lambda'}^{\ell'}(\hat{R}_0) \\ &\times M_{\ell, m; \ell', m'}^{\mathbf{P}L/2\pi}(q), \end{aligned} \quad (\text{A19})$$

where  $\dim \Lambda_{\mathbf{P}}$  gives the dimension of only the elements of  $\Lambda$  with total momentum  $\mathbf{P}$ . Tracing over all irrep indices  $\mu$  makes this expression manifestly invariant under a change of basis of the lattice irreducible representations since under a unitary change of basis,

$$\sum_{\mu} S_{\mu}^* S_{\mu} \rightarrow \sum_{\mu \bar{\mu} \bar{\mu}'} S_{\mu}^* U_{\bar{\mu} \mu}^* U_{\mu \bar{\mu}'} S_{\bar{\mu}'} = \sum_{\mu} S_{\mu}^* S_{\mu}. \quad (\text{A20})$$

Eq. (A19) respects rotational symmetry,

$$\begin{aligned} &\sum_{\bar{m} \bar{s} \bar{m}'} \mathcal{D}_{\bar{m} \bar{m}}^{\ell*}(\hat{R}) \mathcal{D}_{\bar{s} \bar{s}}^{j*}(\hat{R}) \mathcal{D}_{\bar{m}' \bar{m}'}^{\ell'}(\hat{R}) C_{\ell \bar{m}, j \bar{s}, \ell' \bar{m}'} \\ &= C_{\ell m, j s, \ell' m'} \end{aligned} \quad (\text{A21})$$

and

$$\sum_{\bar{m}} \mathcal{D}_{\bar{m} \bar{m}}^{\ell}(\hat{R}) \mathcal{Z}_{\bar{\ell} \bar{m}}^{\mathbf{d}}(s; q) = \mathcal{Z}_{\bar{\ell} \bar{m}}^{\hat{\mathbf{R}} \mathbf{d}}(s; q) = \mathcal{Z}_{\bar{\ell} \bar{m}}^{\mathbf{d}}(s; q) \quad (\text{A22})$$

imply the symmetry

$$\begin{aligned} \mathcal{M}_{\ell, n; \ell', n'}^{\mathbf{P}, \Lambda}(q) &= \mathcal{M}_{\ell, n; \ell', n'}^{\hat{\mathbf{R}} \mathbf{P}, \Lambda}(q) \\ &= \frac{1}{\dim \Lambda_{\mathbf{P}}} \sum_{\mu} \sum_{\lambda, \lambda'} \sum_{m m'} \\ &\times S_{\Lambda^{(n)}, \mu}^{\hat{\mathbf{R}} \mathbf{P}, \ell, \lambda} S_{\Lambda^{(n')}, \mu}^{\hat{\mathbf{R}} \mathbf{P}, \ell', \lambda'} \\ &\times \mathcal{D}_{m\lambda}^{\ell*}(\hat{R} \hat{R}_0) \mathcal{D}_{m'\lambda'}^{\ell'}(\hat{R} \hat{R}_0) \\ &\times M_{\ell, m; \ell', m'}^{\hat{\mathbf{R}} \mathbf{P}L/2\pi}(q), \end{aligned} \quad (\text{A23})$$

with  $\hat{R}$  in the octahedral rotation group  $O_h$ . This symmetry relates momenta that are connected by lattice rotations, so it is not necessary to compute more than one choice of momentum. In general, the momentum  $\mathbf{P}$  cannot be rotated to be parallel to the  $\hat{z}$  axis, so the expression still depends on the direction that  $\mathbf{P}$  is oriented with respect to the lattice axes.

The rotational symmetry of Eq. (A23) implies that the sum over the irrep row is also not necessary to produce a basis-independent result. This is easily seen by noting that, when the sum over  $\mu$  is absent, the expression in Eq. (A19) describes a tensor product in the octahedral

representation,

$$\begin{aligned}
& \sum_{\lambda, \lambda'} \sum_{mm'} S_{\Lambda^{(n)}, \mu}^{\mathbf{P}, \ell, \lambda} * S_{\Lambda^{(n')}, \mu'}^{\mathbf{P}, \ell', \lambda'} \\
& \quad \times \mathcal{D}_{m\lambda}^{\ell *}(\hat{R}_0) \mathcal{D}_{m'\lambda'}^{\ell'}(\hat{R}_0) M_{\ell, m; \ell', m'}^{\mathbf{P}L/2\pi}(q) \\
& = \sum_{\sigma} \sum_{\nu_{\sigma}} \mathcal{M}_{\nu_{\sigma}}^{\bar{\Lambda} \otimes \Lambda \rightarrow \sigma} \langle \Lambda^{(n')}, \mu' | \Lambda^{(n)}, \mu; \sigma, \nu_{\sigma} \rangle \\
& = \mathcal{M}_0^{\bar{\Lambda} \otimes \Lambda \rightarrow A_1} \delta_{\mu\mu'} + (\dots), \tag{A24}
\end{aligned}$$

where

$$\begin{aligned}
\mathcal{M}_{\nu_{\sigma}}^{\bar{\Lambda} \otimes \Lambda \rightarrow \sigma} & = \sum_{\mu\mu'} \sum_{\lambda, \lambda'} \sum_{mm'} S_{\Lambda^{(n)}, \mu}^{\mathbf{P}, \ell, \lambda} * S_{\Lambda^{(n')}, \mu'}^{\mathbf{P}, \ell', \lambda'} \\
& \quad \times \mathcal{D}_{m\lambda}^{\ell *}(\hat{R}_0) \mathcal{D}_{m'\lambda'}^{\ell'}(\hat{R}_0) \\
& \quad \times M_{\ell, m; \ell', m'}^{\mathbf{P}L/2\pi}(q) \langle \Lambda^{(n)}, \mu; \sigma, \nu_{\sigma} | \Lambda^{(n')}, \mu' \rangle \tag{A25}
\end{aligned}$$

denotes the contribution to  $\mathcal{M}$  in Eq. (A19) from irrep  $\sigma$  and the ellipses indicate other nontrivial irrep contributions that all vanish in the gauge average. The trivial  $A_1$  irrep has only one index  $\nu_{A_1} = 0$ . From this point, it is easy to verify that

$$\begin{aligned}
\mathcal{M}_{\ell, n; \ell', n'}^{\mathbf{P}, \Lambda}(q) & = \sum_{\lambda, \lambda'} \sum_{mm'} S_{\Lambda^{(n)}, \mu}^{\mathbf{P}, \ell, \lambda} * S_{\Lambda^{(n')}, \mu}^{\mathbf{P}, \ell', \lambda'} \\
& \quad \times \mathcal{D}_{m\lambda}^{\ell *}(\hat{R}_0) \mathcal{D}_{m'\lambda'}^{\ell'}(\hat{R}_0) M_{\ell, m; \ell', m'}^{\mathbf{P}L/2\pi}(q) \tag{A26}
\end{aligned}$$

independent of  $\mu$ .

When the angular momentum and embedding are fixed with  $\ell = \ell'$  and  $n = n'$ , the sum over the product of subduction coefficients forms a projection matrix. For the cases considered in this manuscript, namely where  $\ell = 0$  in the rest frame, this projection is either the identity matrix or zero with only one possible embedding  $n = n' = 0$ . For these cases, the expression in Eq. (A19) simplifies. Assuming

$$\sum_{\mu} S_{\Lambda, \mu}^{\mathbf{P}, \ell, \lambda} * S_{\Lambda, \mu}^{\mathbf{P}, \ell, \lambda'} = \delta^{\lambda\lambda'}, \tag{A27}$$

the simplified expression is

$$\begin{aligned}
\mathcal{M}_{\ell, 0; \ell, 0}^{\mathbf{P}, \Lambda}(q) & = \sum_{\lambda} \sum_{mm'} \mathcal{D}_{m\lambda}^{\ell *}(\hat{R}_0) \mathcal{D}_{m'\lambda}^{\ell}(\hat{R}_0) M_{\ell, m; \ell, m'}^{\mathbf{d}}(q) \\
& = \sum_m M_{\ell, m; \ell, m}^{\mathbf{P}L/2\pi}(q). \tag{A28}
\end{aligned}$$

- 
- [1] J. R. Batley *et al.* (NA48), *Phys. Lett. B* **544**, 97 (2002), [arXiv:hep-ex/0208009](#).
- [2] E. Abouzaid *et al.* (KTeV), *Phys. Rev. D* **83**, 092001 (2011), [arXiv:1011.0127 \[hep-ex\]](#).
- [3] Z. Bai *et al.* (RBC, UKQCD), *Phys. Rev. Lett.* **115**, 212001 (2015), [arXiv:1505.07863 \[hep-lat\]](#).
- [4] R. Abbott *et al.* (RBC, UKQCD), *Phys. Rev. D* **102**, 054509 (2020), [arXiv:2004.09440 \[hep-lat\]](#).
- [5] T. Blum *et al.* (RBC, UKQCD), *Phys. Rev. D* **104**, 114506 (2021), [arXiv:2103.15131 \[hep-lat\]](#).
- [6] C. Lehner, “The hadronic vacuum polarization contribution to the muon anomalous magnetic moment,” (2016), RBRC Workshop on Lattice Gauge Theories.
- [7] S. Borsanyi, Z. Fodor, T. Kawanai, S. Krieg, L. Lelouch, R. Malak, K. Miura, K. K. Szabo, C. Torrero, and B. Toth, *Phys. Rev. D* **96**, 074507 (2017), [arXiv:1612.02364 \[hep-lat\]](#).
- [8] M. Bruno, T. Izubuchi, C. Lehner, and A. S. Meyer, *PoS LATTICE2019*, 239 (2019), [arXiv:1910.11745 \[hep-lat\]](#).
- [9] T. Aoyama *et al.*, *Phys. Rept.* **887**, 1 (2020), [arXiv:2006.04822 \[hep-ph\]](#).
- [10] A. S. Kronfeld, D. G. Richards, W. Detmold, R. Gupta, H.-W. Lin, K.-F. Liu, A. S. Meyer, R. Sufian, and S. Syritsyn (USQCD), *Eur. Phys. J. A* **55**, 196 (2019), [arXiv:1904.09931 \[hep-lat\]](#).
- [11] M. Luscher, *Commun. Math. Phys.* **105**, 153 (1986).
- [12] M. Luscher, *Nucl. Phys.* **B354**, 531 (1991).
- [13] M. Luscher, *Nucl. Phys.* **B364**, 237 (1991).
- [14] K. Rummukainen and S. A. Gottlieb, *Nucl. Phys.* **B450**, 397 (1995), [arXiv:hep-lat/9503028 \[hep-lat\]](#).
- [15] L. Leskovec and S. Prelovsek, *Phys. Rev. D* **85**, 114507 (2012), [arXiv:1202.2145 \[hep-lat\]](#).
- [16] P. Guo, J. Dudek, R. Edwards, and A. P. Szczepaniak, *Phys. Rev. D* **88**, 014501 (2013), [arXiv:1211.0929 \[hep-lat\]](#).
- [17] A. Woss, C. E. Thomas, J. J. Dudek, R. G. Edwards, and D. J. Wilson, *JHEP* **07**, 043 (2018), [arXiv:1802.05580 \[hep-lat\]](#).
- [18] A. J. Woss, *The scattering of spinning hadrons from lattice QCD*, *Ph.D. thesis*, Cambridge U., DAMTP (2019).
- [19] M. T. Hansen and S. R. Sharpe, *Ann. Rev. Nucl. Part. Sci.* **69**, 65 (2019), [arXiv:1901.00483 \[hep-lat\]](#).
- [20] A. Rusetsky, *PoS LATTICE2019*, 281 (2019), [arXiv:1911.01253 \[hep-lat\]](#).
- [21] M. Mai, M. Döring, and A. Rusetsky, *Eur. Phys. J. ST* **230**, 1623 (2021), [arXiv:2103.00577 \[hep-lat\]](#).
- [22] B. Hörz and A. Hanlon, *Phys. Rev. Lett.* **123**, 142002 (2019), [arXiv:1905.04277 \[hep-lat\]](#).
- [23] M. Fischer, B. Kostrzewa, L. Liu, F. Romero-López, M. Ueding, and C. Urbach, (2020), [arXiv:2008.03035 \[hep-lat\]](#).
- [24] N. Ishii, S. Aoki, and T. Hatsuda, *Phys. Rev. Lett.* **99**, 022001 (2007), [arXiv:nucl-th/0611096](#).
- [25] S. Aoki, T. Hatsuda, and N. Ishii, *Prog. Theor. Phys.*

- 123**, 89 (2010), arXiv:0909.5585 [hep-lat].
- [26] N. Ishii, S. Aoki, T. Doi, T. Hatsuda, Y. Ikeda, T. Inoue, K. Murano, H. Nemura, and K. Sasaki (HAL QCD), *Phys. Lett. B* **712**, 437 (2012), arXiv:1203.3642 [hep-lat].
- [27] D. Kawai, S. Aoki, T. Doi, Y. Ikeda, T. Inoue, T. Iritani, N. Ishii, T. Miyamoto, H. Nemura, and K. Sasaki (HAL QCD), *PTEP* **2018**, 043B04 (2018), arXiv:1711.01883 [hep-lat].
- [28] M. Peardon, J. Bulava, J. Foley, C. Morningstar, J. Dudek, R. G. Edwards, B. Joo, H.-W. Lin, D. G. Richards, and K. J. Juge (Hadron Spectrum), *Phys. Rev. D* **80**, 054506 (2009), arXiv:0905.2160 [hep-lat].
- [29] B. Blossier, M. Della Morte, G. von Hippel, T. Mendes, and R. Sommer, *JHEP* **04**, 094 (2009), arXiv:0902.1265 [hep-lat].
- [30] J. Bulava, B. Fahy, J. Foley, Y.-C. Jhang, K. J. Juge, D. Lenkner, C. Morningstar, and C. H. Wong, *EPJ Web Conf.* **73**, 03018 (2014), arXiv:1401.2544 [hep-lat].
- [31] M. Fischer, B. Kostrzewa, J. Ostmeier, K. Ottnad, M. Ueding, and C. Urbach, *Eur. Phys. J. A* **56**, 206 (2020), arXiv:2004.10472 [hep-lat].
- [32] J. J. Dudek, R. G. Edwards, and C. E. Thomas, *Phys. Rev. D* **86**, 034031 (2012), arXiv:1203.6041 [hep-ph].
- [33] S. R. Sharpe, R. Gupta, and G. W. Kilcup, *Nucl. Phys. B* **383**, 309 (1992).
- [34] R. Gupta, A. Patel, and S. R. Sharpe, *Phys. Rev. D* **48**, 388 (1993), arXiv:hep-lat/9301016.
- [35] Y. Kuramashi, M. Fukugita, H. Mino, M. Okawa, and A. Ukawa, *Phys. Rev. Lett.* **71**, 2387 (1993).
- [36] J. Tu, *Lattice QCD Simulations towards Strong and Weak Coupling Limits*, Ph.D. thesis, Columbia U. (2020).
- [37] T. Blum *et al.* (RBC, UKQCD), *Phys. Rev. D* **93**, 074505 (2016), arXiv:1411.7017 [hep-lat].
- [38] P. M. Vranas, *NATO Sci. Ser. C* **553**, 11 (2000), arXiv:hep-lat/0001006.
- [39] P. M. Vranas, *Phys. Rev. D* **74**, 034512 (2006), arXiv:hep-lat/0606014.
- [40] H. Fukaya, S. Hashimoto, K.-I. Ishikawa, T. Kaneko, H. Matsufuru, T. Onogi, and N. Yamada (JLQCD), *Phys. Rev. D* **74**, 094505 (2006), arXiv:hep-lat/0607020.
- [41] D. Renfrew, T. Blum, N. Christ, R. Mawhinney, and P. Vranas, *PoS LATTICE2008*, 048 (2008), arXiv:0902.2587 [hep-lat].
- [42] E. Shintani, R. Arthur, T. Blum, T. Izubuchi, C. Jung, and C. Lehner, *Phys. Rev. D* **91**, 114511 (2015), arXiv:1402.0244 [hep-lat].
- [43] M. Tanabashi *et al.* (Particle Data Group), *Phys. Rev. D* **98**, 030001 (2018).
- [44] J. J. Dudek, R. G. Edwards, M. J. Peardon, D. G. Richards, and C. E. Thomas, *Phys. Rev. Lett.* **103**, 262001 (2009), arXiv:0909.0200 [hep-ph].
- [45] T. Blum *et al.* (RBC, UKQCD), *Phys. Rev. D* **93**, 074505 (2016), arXiv:1411.7017 [hep-lat].
- [46] R. D. Mawhinney and D. J. Murphy (RBC-UKQCD), *PoS LATTICE2015*, 061 (2016), arXiv:1511.04419 [hep-lat].
- [47] P. A. Boyle *et al.*, *Phys. Rev. D* **93**, 054502 (2016), arXiv:1511.01950 [hep-lat].
- [48] S. M. Roy, *Phys. Lett. B* **36**, 353 (1971).
- [49] B. Ananthanarayan, G. Colangelo, J. Gasser, and H. Leutwyler, *Phys. Rept.* **353**, 207 (2001), arXiv:hep-ph/0005297.
- [50] G. Colangelo, J. Gasser, and H. Leutwyler, *Nucl. Phys. B* **603**, 125 (2001), arXiv:hep-ph/0103088.
- [51] I. Caprini, G. Colangelo, and H. Leutwyler, *Eur. Phys. J. C* **72**, 1860 (2012), arXiv:1111.7160 [hep-ph].
- [52] (RBC, UKQCD), In preparation.
- [53] Y. Aoki *et al.*, (2021), arXiv:2111.09849 [hep-lat].
- [54] M. Mai, C. Culver, A. Alexandru, M. Döring, and F. X. Lee, *Phys. Rev. D* **100**, 114514 (2019), arXiv:1908.01847 [hep-lat].
- [55] Z. Fu and X. Chen, *Phys. Rev. D* **98**, 014514 (2018), arXiv:1712.02219 [hep-lat].
- [56] L. Liu *et al.*, *Phys. Rev. D* **96**, 054516 (2017), arXiv:1612.02061 [hep-lat].
- [57] Z. Fu, *Phys. Rev. D* **87**, 074501 (2013), arXiv:1303.0517 [hep-lat].
- [58] C. Helmes, C. Jost, B. Knippschild, C. Liu, J. Liu, L. Liu, C. Urbach, M. Ueding, Z. Wang, and M. Werner (ETM), *JHEP* **09**, 109 (2015), arXiv:1506.00408 [hep-lat].
- [59] K. Sasaki, N. Ishizuka, M. Oka, and T. Yamazaki (PACS-CS), *Phys. Rev. D* **89**, 054502 (2014), arXiv:1311.7226 [hep-lat].
- [60] S. R. Beane, E. Chang, W. Detmold, H. W. Lin, T. C. Luu, K. Orginos, A. Parreno, M. J. Savage, A. Torok, and A. Walker-Loud (NPLQCD), *Phys. Rev. D* **85**, 034505 (2012), arXiv:1107.5023 [hep-lat].
- [61] Z. Fu, *Commun. Theor. Phys.* **57**, 78 (2012), arXiv:1110.3918 [hep-lat].
- [62] T. Yagi, S. Hashimoto, O. Morimatsu, and M. Ohtani, (2011), arXiv:1108.2970 [hep-lat].
- [63] X. Feng, K. Jansen, and D. B. Renner, *Phys. Lett. B* **684**, 268 (2010), arXiv:0909.3255 [hep-lat].
- [64] S. R. Beane, T. C. Luu, K. Orginos, A. Parreno, M. J. Savage, A. Torok, and A. Walker-Loud, *Phys. Rev. D* **77**, 014505 (2008), arXiv:0706.3026 [hep-lat].
- [65] S. R. Beane, P. F. Bedaque, K. Orginos, and M. J. Savage (NPLQCD), *Phys. Rev. D* **73**, 054503 (2006), arXiv:hep-lat/0506013.
- [66] T. Blum, P. A. Boyle, V. Gülpers, T. Izubuchi, L. Jin, C. Jung, A. Jüttner, C. Lehner, A. Portelli, and J. T. Tsang (RBC, UKQCD), *Phys. Rev. Lett.* **121**, 022003 (2018), arXiv:1801.07224 [hep-lat].
- [67] C. E. Thomas, R. G. Edwards, and J. J. Dudek, *Phys. Rev. D* **85**, 014507 (2012), arXiv:1107.1930 [hep-lat].
- [68] J. J. Dudek, R. G. Edwards, M. J. Peardon, D. G. Richards, and C. E. Thomas, *Phys. Rev. D* **82**, 034508 (2010), arXiv:1004.4930 [hep-ph].